A TOPBP1 Allele Causing Male Infertility Uncouples XY Silencing Dynamics From Sex Body Formation

Carolline F. R. Ascencao[1*], Jennie R. Sims[1*], Alexis Dziubek[1], William Comstock[1], Elizabeth A. Fogarty[1], Jumana Badar[1], Raimundo Freire[2,3,4], Andrew Grimson[1], Robert S. Weiss[5], Paula E. Cohen[5,#] and Marcus Smolka[1,#]

1. Department of Molecular Biology and Genetics, Cornell University, United States;
2. Fundación Canaria del Instituto de Investigación Sanitaria de Canarias (FIISC), Unidad de Investigación, Hospital Universitario de Canarias, La Laguna, Santa Cruz de Tenerife, Spain;
3. Instituto de Tecnologías Biomédicas, Universidad de La Laguna, 38200 La Laguna, Spain;
4. Universidad Fernando Pessoa Canarias, Las Palmas de Gran Canaria, Spain;
5. Department of Biomedical Sciences, Cornell University, United States.

* Contributed equally

\# Co-corresponding authors

ABSTRACT

Meiotic sex chromosome inactivation (MSCI) is a critical feature of meiotic prophase I progression in males. While the ATR kinase and its activator TOPBP1 are key drivers of MSCI within the specialized sex body (SB) domain of the nucleus, how they promote silencing remains unclear given their multifaceted meiotic functions that also include DNA repair, chromosome synapsis and SB formation. Here we report a novel mutant mouse harboring mutations in the TOPBP1-BRCT5 domain. *Topbp1*$^{B5/B5}$ males are infertile, with impaired MSCI despite displaying grossly normal events of early prophase I, including synapsis and SB formation. Specific ATR-dependent events are disrupted including phosphorylation and localization of the RNA:DNA helicase Senataxin. *Topbp1*$^{B5/B5}$ spermatocytes initiate, but cannot maintain ongoing, MSCI. These findings reveal a non-canonical role for the ATR-TOPBP1 signaling axis in MSCI dynamics at advanced stages in pachynema and establish the first mouse mutant that separates ATR signaling and MSCI from SB formation.

Introduction

During Prophase I, the SPO11 nuclease and its cofactors induce programmed DNA double-strand breaks (DSBs) that are then recognized by the DNA damage response (DDR) machinery to promote recombination between homologous chromosomes[1–4]. Proper chromosome synapsis achieved through the formation of the proteinaceous synaptonemal complex, together with homologous recombination (HR)-mediated DNA repair[5] are critical for the formation of crossovers that ensure the correct segregation of chromosomes and the formation of healthy and genetically diverse haploid gametes[6]. Chromosomes that fail to synapse as prophase I progresses trigger a process referred to as meiotic silencing of unsynapsed chromatin (MSUC)[7–10] to silence genes at unsynapsed regions. In the heterogametic sex (male mammals), the X and Y chromosomes pose a unique challenge for meiotic progression since they bear homology only at the pseudoautosomal region (PAR). The non-homologous arms of the sex chromosomes remain unsynapsed and must therefore undergo a sex-chromosome specific manifestation of MSUC, termed meiotic sex-chromosome inactivation (MSCI)[8,11–13]. MSCI is critical for normal prophase I progression through two complementary mechanisms, the silencing of toxic Y-linked genes, such as *Zfy1* and *Zfy2*, that enforce the pachytene checkpoint[13,14] and through the sequestration of the DDR machinery at the X and Y chromosomes, away from the autosomes, during early pachynema[10].

The apical serine-threonine kinase Ataxia Telangiectasia mutated and Rad-3 related (ATR), is a master regulator of DNA repair, checkpoints and silencing during prophase I in spermatocytes. In response to DSBs and asynapsis, ATR activation promotes a range of downstream effects, including recombinational DNA repair, crossing over, chromosome synapsis, cell cycle arrest and potentially apoptosis[5,15–18]. During leptonema and zygonema, shortly after DSB formation, ATR and its cofactor ATRIP are recruited to RPA-coated regions of single strand DNA (ssDNA) that accumulate upon 5’-3’ resection of both ends of DSBs[19]. ATR activation requires recruitment of TOPBP1 (topoisomerase 2 binding protein 1), a multi-BRCT (BRCA C-terminus motif) domain protein that stimulates ATR kinase activity through its ATR-activation domain (AAD)[19–21]. In addition to activating ATR, TOPBP1 also serves as a scaffold for a range of DDR factors, interacting with, and often recruiting them via its multiple BRCT domains[22–29]. TOPBP1 is

composed of nine BRCT domains, which are protein-interacting modules that typically recognize phosphorylated motifs[22,30,31]. Through the recognition of phosphoproteins, TOPBP1 is able to assemble multisubunit complexes to promote discrete pathways[5,22–29,32–34]. TOPBP1 interacts with the C-terminal tail of RAD9, a component of the 9-1-1 PCNA-like clamp that is loaded at 5' recessed junctions adjacent to DSBs[35]. The 9-1-1-TOPBP1 complex is essential for canonical ATR signaling during prophase I[32–34]. Interaction of a protein with TOPBP1 may facilitate its phosphorylation by ATR[19], suggesting a potential role for TOPBP1 in the control of ATR substrate selection[19]. How the 9-1-1-TOPBP1-ATR signaling axis and the different TOPBP1 interactions coordinate DNA repair, checkpoints and silencing during meiosis remains incompletely understood.

As cells progress from zygonema into pachynema, ATR and TOPBP1 localize to the unsynapsed axes of the X and Y chromosomes[36–38], leading to phosphorylation of the histone variant H2AX on serine 139 (γH2AX), a major hallmark of MSCI[16,18]. During establishment of MSCI, a phase separated structure termed the sex body is formed[39], allowing the confinement of ATR signaling, DDR factors and silencing to the X and Y[10,11] as part of a checkpoint that induces cell death if DDR proteins aberrantly accumulate and remain on autosomes[10]. Recruitment of ATR and TOPBP1 to unsynapsed regions of the XY requires a distinct set of factors compared to their mode of recruitment to autosomal DSB sites mentioned above, and involves factors such as BRCA1 and HORMAD[40,41]. Activated ATR phosphorylates H2AX at the unsynapsed cores of the X and Y chromosomes, a signaling that is propagated to chromatin loops of the X and Y, via a feed-forward process mediated by recruitment of the MDC1 adaptor, which further recruits and mobilizes additional TOPBP1-ATR complexes, therefore spreading ATR signaling to promote the broad chromosome-wide silencing required for MSCI[42]. It has also been proposed that the initiation of MSCI sequesters DDR proteins from autosomes to the X and Y chromosomes to prevent excessive DDR signaling at autosomes from activating cellular checkpoints that can stop meiotic progression[10].

Despite mounting evidence pointing to the importance of ATR and TOPBP1 for MSCI, the precise mechanisms by which they promote sex body formation and XY silencing remain unknown. Moreover, it remains unclear how these two processes are spatiotemporally coordinated and how

ATR and TOPBP1 mediate such coordination. Since both proteins are essential for organismal viability[43–49], conditional knockouts[16,18,34] or hypomorphic[15] models have been used to explore their roles during prophase I in spermatocytes. However, given the strong pleiotropic effects in these models, especially in DSB repair, synapsis, MSCI and sex body formation, it is difficult to dissect the distinct molecular mechanisms involved, and to untangle direct versus indirect effects. Here we present a separation-of-function mouse mutant that deconvolutes TOPBP1-dependent ATR signaling in male meiosis. We generated mice bearing multiple mutations in BRCT-domain 5 (*Topbp1*$^{B5/B5}$ mice) that are viable and grossly indistinguishable from wild-type littermates; yet, the males are sterile, having reduced testes size, reduced seminiferous tubule cellularity, and a complete loss of sperm. Strikingly, while *Topbp1*$^{B5/B5}$ spermatocytes fail to progress into diplotene, they display largely normal chromosome synapsis, sex body formation, recruitment of DDR proteins to the X and Y, and DNA repair during prophase I, in sharp contrast to previous models of TOPBP1 or ATR impairment[18,34]. Single-cell RNA sequencing data showed that while MSCI is initiated in *Topbp1*$^{B5/B5}$, the dynamics of silencing progression and reinforcement is defective, which is accompanied by a defect in the localization of the RNA:DNA helicase Senataxin to chromatin loops of the XY chromosomes. We propose that the *Topbp1*$^{B5/B5}$ is a separation of function mutant that allows the untangling of XY silencing from sex body formation and DDR recruitment to the XY, representing a unique model to study the establishment, maintenance, reinforcement and progression of MSCI.

Results

A TOPBP1 mutant separating its role in fertility from organismal viability.

Topbp1 knockout mice exhibit strong defects early in embryonic development, reaching blastocyst stage but not progressing beyond E.8, with embryos likely dying at the preimplantation stage[48]. In the context of meiosis, conditional knockout of *Topbp1* in spermatocytes leads to pleiotropic effects, including defects in chromosome synapsis, impaired recruitment of DDR factors to XY chromosomes, defects in condensation of the XY chromosomes, abnormal formation of the sex body, lack of γH2AX spreading to chromatin loops, all of which contribute to a strong MSCI defect as indicated by the complete absence of downstream markers of MSCI, such as USP7, H3K9me3, poly-ubiquitination and sumoylation[5,34]. The availability of a separation of function mutant for *Topbp1* is therefore needed to dissect its distinct roles in development, organismal maintenance, and multiple meiotic processes such as DNA repair, silencing and sex body formation. To generate a separation of function mouse model, we inserted eight charge reversal point mutations in BRCT domain 5 of TOPBP1 (hereafter referred to as $Topbp1^{B5/B5}$) CRISPR/Cas9 (Figure 1A). After validating the point mutations through Sanger sequencing, (Supplemental Figure 1), we found that $Topbp1^{B5/B5}$ mice were viable, with no difference in body mass when compared to *WT* littermates (Figures 1B and 1C), and no sensitivity to Ionizing Radiation (IR) (Figures 1D). Strikingly, $Topbp1^{B5/B5}$ mice displayed male-specific infertility (Figure 1E), with a three-fold reduction in testis size (Figures 1F and 1G) and complete lack of spermatozoa (Figure 1H). H&E-stained histological testis sections revealed mainly spermatogonia and spermatocytes within the seminiferous epithelium (Figure 1I) together with an increased number of TUNEL-positive spermatocytes in seminiferous tubules (Figure 1J and 1K). Cytological evaluation of surface-spread spermatocytes from $Topbp1^{B5/B5}$ revealed the presence of meiotic prophase I stages from leptonema to pachynema but a total absence of diplonema-staged spermatocytes (Figure 1L). Moreover, the staining of the synaptonemal complex proteins SYCP1 and SYCP3 revealed normal pachytene entry and no gross defects in chromosome synapsis, distinct from previous models of ATR and TOPBP1 conditional depletion[18,34]. Furthermore, unlike reported DDR CKO (conditional knockouts) models such as *Rad1* and *Brca1*[10,29,36], $Topbp1^{B5/B5}$ pachytene spermatocytes reach mid-pachynema, as demonstrated by the accumulation of signal for H1t[50] (Figure 1L).

Topbp1$^{B5/B5}$ MEFs display no detectable DDR defects.

To assess the possibility of a somatic phenotype we derived mouse embryonic fibroblasts (MEFs) from *Topbp1*$^{B5/B5}$ and wild-type littermates at embryonic day E13.5. Consistent with the observed organismal viability and the lack of IR sensitivity, *Topbp1*$^{B5/B5}$ MEFs showed no sensitivity to hydroxyurea (replication stress) or phleomycin (DSBs) in a long-term cell survival assay (Figure 2A-D and Supplemental Figure 2). Genotoxic stress activates the apical kinases ATR, ATM and DNA-PKcs[51–53] to trigger a signaling cascade that promotes DNA repair and cell cycle arrest via activation of the downstream checkpoint kinases CHK1 and CHK2[54–56]. Similar to wild-type MEFs, *Topbp1*$^{B5/B5}$MEFs were able to activate DDR signaling responses when challenged with hydroxyurea and phleomycin as demonstrated by the induction of established damage-induced phosphorylation of CHK1, CHK2, RPA and KAP1 (Figure 2E). In addition, *Topbp1*$^{B5/B5}$ MEFs were able to recruit MDC1 to γH2AX-marked DSB foci when subjected to IR (Figure 2F) and showed no increased number of micronuclei, a known marker of defective DNA damage responses[57], when compared to *Topbp1*$^{+/+}$ MEFs (Supplemental Figure 3A-B).

The BRCT-5 domain of TOPBP1 is known to interact with the DDR factors 53BP1[22,24,28], MDC1[58] and BLM[27] through phospho-protein binding modules. To investigate which, if any, of these interactions are disrupted upon mutating the eight BRCT5 residues, we ectopically expressed Flag-TOPBP1-WT or Flag-TOPBP1-B5 in HEK293T cells. We found that binding of Flag-TOPBP1-B5 to BLM and 53BP1 was impaired, as expected (Supplemental Figure 4A-B). Moreover, we noticed a 2-fold reduction in protein levels of Flag-TOPBP1-B5 compared to Flag-TOPBP1-WT, which could be explained by the loss of interaction with BLM (that was proposed to lead to protein stabilization[59,60]), or by protein misfolding caused by the 8 eight K to E/D mutations. In addition, the reduction in protein levels was detected on MEFs (Supplemental Figure 5). In either case, the results presented here show that the TOPBP1-B5 mutant offers a unique model to separate roles of TOPBP1 in male meiosis from the canonical DDR functions of TOPBP1 in somatic cells.

Topbp1$^{B5/B5}$ spermatocytes display normal markers of canonical ATR signaling, chromosome synapsis, DNA repair, sex body formation, and DDR protein localization at the X and Y

TOPBP1 and ATR play multiple roles in spermatocytes during prophase I. Mice conditionally depleted for TOPBP1[34] or ATR[16,18] display severe defects in chromosome synapsis, DNA DSB repair, sex body formation and MSCI, as well as impaired recruitment of DDR factors to the XY[5]. Strikingly, analysis of *Topbp1*$^{B5/B5}$ spermatocytes via meiotic spreads revealed normal repair of DNA DSBs, with γH2AX staining grossly unchanged at pachynema, being confined only to the XY chromosomes and being excluded from the autosomes (Figure 3A-B). RAD51 localized only to the X and Y chromosomes during mid-pachytene (Figure 3C-D), indicating normal DSB repair at the autosomes. We were unable to detect chromosome synapsis abnormalities in *Topbp1*$^{B5/B5}$ spermatocytes, as *Topbp1*$^{B5/B5}$ mutant spermatocytes transit from zygotene into pachytene with normal patterns of HORMAD1 and HORMAD2 localization (Supplemental Figure 6A-B) and with SYCP1 overlapping with SYCP3 on chromosome cores from all autosomal chromosomes during pachynema (Figures 1L and 3E). Since ATR orthologs regulate crossing over in budding yeast [1] and in *Drosophila melanogaster* [61], we also investigated the localization of factors involved in regulating DNA crossovers, including MLH1 and MLH3. In *Topbp1*$^{B5/B5}$ spermatocytes, while the number of MLH1 foci were significantly increased, the number of MLH3 foci did not differ significantly (Supplemental Figure 7A and 7B). Due to the lack of diplotene cells, and any other stage after pachynema, we were not able to test whether *Topbp1*$^{B5/B5}$ display defects in crossing over.

The sex body appeared normal in its shape and was normally formed in *Topbp1*$^{B5/B5}$ spermatocytes (Figures 3A and Supplemental Figures 8 and 9A), exhibiting only subtle defects/delays in the spreading of the γH2AX signal on the PAR and pericentromeric regions (Supplemental Figure 9B-G). Although the defect was subtle in its severity, it accounted for 56% of all γH2AX-stained mid-pachytene cells. Importantly, TOPBP1 was normally localized to X and Y chromosomes during prophase I (Supplemental Figure 10 and Figure 3F-H). Similarly, localization of the TOPBP1 interactors ATR, BRCA1, MDC1, and 53BP1 in *Topbp1*$^{B5/B5}$ spermatocytes spreads was also indistinguishable from that observed in *Topbp1*$^{+/+}$ spermatocytes (Figures 4A-F and Supplemental Figures 11). Markers of ATR signaling were also mostly normal, as measured by its canonical targets pMDC1 T4 (Supplemental Figure 6C-D), pCHK1 S345 (Supplemental Figure 6E-F), and pHORMAD2 (Supplemental Figure 6G-H). Notably, we did observe that phosphorylation of CHK1 on S317 was significantly decreased in *Topbp1*$^{B5/B5}$ when compared to *Topbp1*$^{+/+}$

spermatocytes (Figure 4G-H). However, since *Chk1* CKO spermatocytes complete prophase I and differentiate into spermatozoa, with only minor defects such a delay in the removal of γH2AX from autosomes[62], the observed defect in Chk1 S317 phosphorylation is unlikely to be the cause of the infertility observed in *Topbp1* B5 mutants. Overall, as summarized in Figure 4I, *Topbp1*$^{B5/B5}$ spermatocytes appear to progress normally through early stages of prophase I up until the end of pachynema as demonstrated by largely normal localization of markers for DNA repair, chromosome synapsis and ATR signaling. These findings are surprising because the lack of sex body formation, synapsis defects or unrepaired DSBs, which are the expected causes of the drastic loss of diplotene cells and the lack of spermatozoa, were not observed.

Defective phosphorylation and XY localization of the RNA:DNA helicase SETX in *Topbp1*$^{B5/B5}$ spermatocytes

With the exception of CHK1 phosphorylation at serine 317, the analysis of other canonical markers of ATR signaling on meiotic prophase I spreads did not reveal obvious defects in their distribution or intensity at the XY body (Figure 4G-H and Supplemental Figure 6C-H). Since altered CHK1 regulation is unlikely to be the cause of the drastic defect in meiotic progression observed in *Topbp1*$^{B5/B5}$ males, we investigated whether other branches of ATR signaling were altered in *Topbp1*$^{B5/B5}$ spermatocytes by performing unbiased quantitative phosphoproteomics based on TMT (Tandem Mass Tag[63]) labeling of whole testes. Following a similar approach previously used by our group[64], we analyzed the phosphoproteome of *Topbp1*$^{B5/B5}$ and *Topbp1*$^{+/+}$ testes, and then compared the results to our previously reported dataset comparing the phosphoproteome of testes from mice treated with vehicle or the ATR inhibitor AZ20[64] (Figure 5A). The resulting plot revealed that ATR-dependent signaling is not drastically impaired in *Topbp1*$^{B5/B5}$ testes, as opposed to the marked impairment of ATR signaling previously observed in testes of *Rad1* CKO mice[64]. This finding is in agreement with the results from meiotic spreads of *Topbp1*$^{B5/B5}$ showing no detectable defects in canonical markers of ATR signaling described above. Nonetheless, our phosphoproteomic analysis did reveal phosphorylation sites mildly disrupted in *Topbp1*$^{B5/B5}$ testes compared to *Topbp1*$^{+/+}$ testes. In particular, we noticed that several phosphorylation sites in the RNA:DNA helicase, Senataxin (SETX)[65], including a phosphorylation in the preferred motif for ATR phosphorylation (S/T-Q), were down-regulated in *Topbp1*$^{B5/B5}$ mice (Figure 5B). Interestingly, SETX was previously associated with meiotic ATR functions[66,67] and found to be

indispensable for MSCI[66,67]. Moreover, we recently reported that mice treated with the ATR inhibitor AZ20 or lacking *Rad1* display reduced phosphorylation of SETX at S/T-Q site and SETX mislocalization during pachynema[64]. Based on our findings, we propose that TOPBP1 regulates SETX distribution and/or function during meiosis, and that defects in meiotic progression and fertility observed in *Topbp1*$^{B5/B5}$ mice might be associated with SETX dysfunction. Consistent with this possibility, we found that pachytene spermatocytes from *Topbp1*$^{B5/B5}$ display significantly decreased spreading of SETX to XY chromatin loops while still displayed SETX at the unsynapsed axes of the X and Y chromosomes (Figures 5C-F). Overall, these findings reveal that *Topbp1*$^{B5/B5}$ spermatocytes display largely normal progression through mid-pachynema, as demonstrated by normal distribution of a range of markers of meiotic progression, including canonical markers of ATR signaling. However, in-depth phosphoproteomic and imaging analyses identify specific defects in the regulation of SETX, a target of ATR signaling during prophase I[29,64] and a key factor required for MSCI[66,67].

Topbp1$^{B5/B5}$ spermatocytes initiate MSCI but fail to promote full XY silencing

During mid-pachynema, spermatocytes that fail to properly silence the X and Y chromosomes arrest and trigger apoptosis-induced cell death[9–11,68]. In mice, the MSCI process initiates in leptonema[69], and during early pachynema key events occur at the XY chromosomes, such as exclusion of RNA polymerase 2 (RNA Pol2), recruitment of DDR proteins and chromatin remodelers and establishment of heterochromatin marks[10,70] to maintain the active silencing of the X and Y chromosomes[17]. This process leads to the formation of a membrane-less phase separated structure termed the sex body[39,71]. Spermatocytes from *Topbp1*$^{B5/B5}$ males formed a sex body of grossly normal appearance (Supplemental Figure 8), with undisrupted patterns of the sex body markers CHD4, SUMO, and USP7 (Supplemental Figure 12). *Topbp1*$^{B5/B5}$ pachytene spermatocytes also display normal patterns of a range of chromatin marks, including H3K9ac, H3K9me3, H3K27ac, H3K36me3, H3K4me3, H4K16ac, H4ac, H2AK116ub, H3K4me1, as well as proper exclusion of RNA Pol2 from the sex body (Supplemental Figures 13-17). Collectively the evidence presented herein shows that *Topbp1*$^{B5/B5}$ mutants are able to form grossly normal XY bodies, with proper localization of over 28 markers, the severe loss of diplotene cells and the reduction of SETX at the chromatin loops of the X and Y lead us to speculate that *Topbp1*$^{B5/B5}$ spermatocytes may still have a defective MSCI. To investigate potential MSCI defects, we

employed single cell RNA sequencing (sc-RNA-seq) in germ cells (Figure 6A) using a similar approach recently used to follow spermatogenesis progression and to evaluate MSCI in mammals[69,72,73]. Using the 10X platform we performed sc-RNA-seq on a germ cell-enriched population of cells extracted from adult *Topbp1*$^{+/+}$ and *Topbp1*$^{B5/B5}$ testes (Figure 6A). The data were analyzed as previously described[69,73] using signature genes as markers of different stages in spermatogenesis such as, *Sal4* and *Dmrt1* for spermatogonia, *Dazl* for early spermatocytes, *Id4*, *Sycp3* and *Shcbp1l* for late spermatocytes, *Acrv1* for round spermatids, and *Oaz3* and *Prm2* for elongated spermatids (Supplemental Figures 18 and 19). *Col1a2*, *Acta2*, *Vcam1*, *Lnsl3*, *laptm5*, *Hbb-bt*, *Ptgds* and *Wt1* were used as markers of somatic cells (Supplemental Figure 20). Analysis of the testicular transcriptome of *Topbp1*$^{+/+}$ males revealed 47 sub-clusters of cells covering spermatogonia, spermatocytes, spermatids, and somatic cells (Figure 6B-D and Supplemental Figures 21-22). In sharp contrast, analysis of *Topbp1*$^{B5/B5}$ germ cell population revealed only somatic, spermatogonia and the initial populations of spermatocytes (Figure 6D). This result corroborates the H&E-stained testes histological sections (Figure 1I) and meiotic spreads (Figure 1L). Importantly, Pearson correlation values from all RNA reads between cell groups separated by cluster and genotype, demonstrated the similarity of spermatocytes from *Topbp1*$^{+/+}$ and *Topbp1*$^{B5/B5}$ (Supplemental Figure 23). As shown in Figure 6E, we were able to monitor the dynamics of X chromosome silencing in the early-stage spermatocytes and compare the results between RNA from *Topbp1*$^{+/+}$ and *Topbp1*$^{B5/B5}$ males. Strikingly, *Topbp1*$^{B5/B5}$ early-stage spermatocytes could initiate MSCI and promote robust, albeit incomplete, X chromosome silencing. Both X and Y chromosomes showed increased gene expression levels in the last spermatocyte stage captured in *Topbp1*$^{B5/B5}$ males when compared to RNA from wild type males (Figure 6E and Supplemental Figure 24). Moreover, although certain X-genes from *Topbp1*$^{B5/B5}$ pachytene cells consistently demonstrated defects in silencing by being expressed in numerous cells, other genes were only expressed in a small number of cells. This highlights the non-uniformity of the MSCI defect in all pachytene cells (Supplemental Figure 24).

MSCI is a dynamic process that involves the sequestration of DDR factors from the autosomes to the X and Y chromosomes as cells enter pachynema[10,17] as well as the inactivation of specific X and Y genes that lead to cell death if expressed at this stage (the so called "killer genes")[13,14]. Similar to previous reports based on mutants or treatments that impaired MSCI[16–18,29,34,74,75],

transcriptomics profiles from *Topbp1*$^{B5/B5}$ testicular cells showed an increased number of stage 3 spermatocytes (SP3 - pachytene) expressing the killer genes *Zfy1* and *Zfy2* compared to *Topbp1*$^{+/+}$ (Supplemental Figures 25-26). Other genes typically used to illustrate MSCI defects, such as *Kdm6a*, *lamp2*, *Zfx*, *Uba1y* and *Rhox13* were also expressed in a higher number of SP3 cells in *Topbp1*$^{B5/B5}$ (Supplemental Figures 25-26). In the case of *Scml2*, *Topbp1*$^{B5/B5}$ cells not only displayed an increased number of SP3 (pachytene) cells expressing it but also displayed an increase in expression levels in these cells compared to *Topbp1*$^{+/+}$ testes (Supplemental Figures 25-26). In summary, various Y and X genes that had previously been shown to be expressed in other MSCI-defective mutants were found de-repressed in *Topbp1*$^{B5/B5}$ spermatocytes.

Detailed analysis of the scRNA-seq data for the X-linked genes monitored during the early spermatocyte stages revealed important differences in the silencing dynamics of these X genes between *Topbp1*$^{B5/B5}$ and *Topbp1*$^{+/+}$ spermatocytes. 233 out of the roughly 700 genes present on the X chromosome had reads detected from pre-leptotene to spermatocyte 3 clusters for both *Topbp1*$^{+/+}$ and *Topbp1*$^{B5/B5}$ cells, and therefore were used during the downstream analysis. As shown in Figure 7A, we clustered the X-linked genes into 3 distinct categories based on the change of RNA level between the stages: reduced, unaltered, or increased silencing (Figures 7A). SP1 (spermatocyte 1) was defined as leptotene using the gene marker *Gm960*[76] (Supplemental Figure 27), and SP2 (spermatocyte 2) as zygotene due to its profile of low expression of *Gm960* and high expression of *Dazl*. SP3 (spermatocyte 3) was defined as pachytene due to its lower expression of *Dazl* and increased expression of *Id4* and *Shcbp1l*. When comparing the distribution of genes in these clusters between *Topbp1*$^{B5/B5}$ and *Topbp1*$^{+/+}$ spermatocytes (RNA level normalized to pre-leptotene stage) (Figure 7B), we observed no major differences in the pre-leptotene to spermatocyte 1 (PL to SP1) and in the spermatocyte 1 to spermatocyte 2 (SP1 to SP2) transitions. In contrast, when comparing the spermatocyte 2 to spermatocyte 3 (SP2 to SP3) transition between *Topbp1*$^{B5/B5}$ and *Topbp1*$^{+/+}$ spermatocytes we noticed a major difference in the distribution of the clusters, with 74 genes in *Topbp1*$^{B5/B5}$ versus 4 in *Topbp1*$^{+/+}$ exhibiting reduced silencing (Figure 7B). Moreover, while 134 genes showed unaltered silencing, and only 24 increased silencing in *Topbp1*$^{B5/B5}$ spermatocytes during the SP2 to SP3 transition, 43 genes showed unaltered silencing and 185 increased silencing in *Topbp1*$^{+/+}$ (Figure 7B). *Xiap*, *Zc3h12b* and *Cetn2* are examples of X-linked genes displaying altered silencing behaviors in *Topbp1*$^{B5/B5}$ spermatocytes (Figure 7C).

The difference of expression between *Topbp1*$^{+/+}$and *Topbp1*$^{B5/B5}$ was markedly higher in the SP2 to SP3 transition compared to the other transitions (Figure 7D-E) and was used to further split genes into 3 categories based on the severity of the silencing defect in *Topbp1*$^{B5/B5}$: no defect (13 genes), mild (45 genes) or strong defect (170 genes) (Figure 7F). Notably, the severity of the silencing defect of a gene had some correlation with its RNA level in the pre-leptotene stage, with highly expressed genes having a higher tendency to have a more severe silencing defect (Figure 7G and Supplemental Figure 28). Taken together, these data characterize the specific silencing defect in *Topbp1*$^{B5/B5}$ spermatocytes and point to a specific role for TOPBP1 in ensuring proper silencing dynamics after an initial wave of MSCI, likely through later waves of silencing reinforcement. Our data is consistent with the notion that silencing of the X and Y chromosomes is a dynamic process that needs active and continuous engagement by the ATR-TOPBP1 signaling axis. Since the majority of the mouse models of male infertility accumulate pleiotropic defects, with disrupted MSCI and absence of sex body, the *Topbp1*$^{B5/B5}$ mouse reported here provides a unique model of DDR impairment in which MSCI can be uncoupled from sex body formation (Figure 8).

Discussion

In male meiosis I, DDR factors such as ATR, TOPBP1, BRCA1, and the 9-1-1 complex play crucial roles in DNA repair, chromosome synapsis, recombination, sex body formation, and silencing[5,15,16,18,29,34,36,40]. Conditional depletion of these factors results in pleiotropic phenotypes from compound effects in multiple processes, with cells ultimately undergoing apoptotic-induced cell death during the pachytene checkpoint. Here, we report a mutant mouse model capable of deconvoluting TOPBP1's roles during meiosis I in males, separating its role in silencing from its roles in DNA repair, synapsis and checkpoint signaling (Figure 8). While *Topbp1*$^{B5/B5}$ spermatocytes initiate XY silencing with similar dynamics as observed in *Topbp1*$^{+/+}$, these cells fail to complete silencing at the final steps of MSCI. Furthermore, not all X genes in *Topbp1*$^{B5/B5}$ spermatocytes were silenced; instead, some genes were only partially silenced while others exhibited increased expression after initial silencing. Interestingly, a sex body is formed that is morphologically indistinguishable from the sex body in wild-type animals. Several heterochromatin markers, as well as multiple canonical markers of sex body formation localize properly in the sex body of *Topbp1*$^{B5/B5}$ mice. Overall, these findings suggest a non-canonical role for the ATR-TOPBP1 signaling axis in ensuring proper XY silencing dynamics during pachynema. This is the first DDR mutant that separates XY silencing from sex body formation, and that separates TOPBP1's role in spermatogenesis from its roles in organismal viability.

The *B5* allele reported here, which carries eight lysine to glutamic/aspartic acid substitutions in BRCT domain 5, is the first mutation shown to impair the meiotic silencing function of TOPBP1 in spermatocytes without severely disturbing TOPBP1's role in synapsis and sex body formation. Consistent with this being a separation of function mutant, *Topbp1*$^{B5/B5}$ males are viable and grossly normal, while completely sterile, whereas *Topbp1* null, or AAD mutated, mice are embryonic lethal[48,49]. Moreover, depletion of TOPBP1 in mammalian cell lines triggers a robust G2/M arrest followed by cell senescence and loss of viability[48] *Topbp1*$^{B5/B5}$ MEFs do not display issues with cell proliferation or DDR defects. Based on these observations, and the finding of a silencing defect in *Topbp1*$^{B5/B5}$ spermatocytes, it is likely that the role of TOPBP1 in silencing documented here could be specifically relevant in the context of male meiosis. It is important to note that other mutants previously reported to have XY silencing defects during meiotic prophase

I, such as *Ago4* null and *Dicer* CKO, do not result in complete loss of sperm production, but a sub-fertility phenotype[75,77]. Therefore, we speculate that the specific type of silencing defect in *Topbp1*$^{B5/B5}$ spermatocytes is particularly toxic, similar to other mutations in the DDR pathway that result in MSCI defects, which would explain the highly penetrant defect in sperm production.

The model that distinct TOPBP1 interactions mediate distinct ATR signaling pathways offers a potential explanation for why *Topbp1*$^{B5/B5}$ have specific defects in silencing without noted effects in other key processes regulated by ATR, such as synapsis. In addition to binding and activating ATR through its AAD domain[5,21], TOPBP1 can bind to several proteins through its BRCT domains[47] and act as a scaffolding protein to bring substrates in close proximity to ATR, thus facilitating the propagation of specific ATR signaling pathways. Experiments using ectopic expression of Flag-tagged TOPBP1 in HEK293T cells revealed that the set of mutations in *B5* disrupt the ability of TOPBP1 to interact with 53BP1 and BLM, as expected from previous reports[22,24,27,28,60]. However, it is unclear if the same interactions are also disrupted in spermatocytes, or whether additional TOPBP1 interactions mediated by its BRCT5 specifically during meiotic prophase I are also disrupted. Apart from disrupting protein interactions, it is also possible that the observed changes in TOPBP1 protein stability in the *Topbp1 B5* mutant can contribute to impairing its roles in silencing. Such change in protein stability is consistent with a previous report showing that the TOPBP1-BLM interaction contributes to protein stabilization[59,60]. Further work will be necessary to determine if the phenotypes observed in *Topbp1*$^{B5/B5}$ spermatocytes are caused specifically by disruption of specific protein interactions, or by a combination of disrupted interactions and reduced protein abundance. It is worth mentioning that the *Topbp1*$^{B5/B5}$ phenotype is distinct from the *Topbp1* CKO despite the reduction in protein abundance.

Our finding that SETX localization to chromatin loops of the XY is impacted in *Topbp1*$^{B5/B5}$ pachytene spermatocytes, together with our previous report that SETX undergoes ATR-dependent phospho-regulation in spermatocytes, suggest that an ATR-TOPBP1-SETX signaling axis is important for the silencing reinforcement in late MSCI. Genetic data support that impairment of this specific signaling axis would impact silencing without impacting synapsis. For example, *Topbp1* CKO, *Rad1* CKO, and *Atr* CKO spermatocytes display strong synapsis defect and

defective entry in pachynema[18,34], whereas *Setx* null spermatocytes complete autosomal synapsis, while still displaying MSCI defects. On the other hand, is it likely that ATR signaling is controlling a specific aspect of SETX function since *Topbp1*$^{B5/B5}$ spermatocytes do not share all defects observed in *Setx* null spermatocytes, as noted by the localization of γH2AX, sumoylation events, ubH2A and ATR at chromatin loops, which are defective in *Setx* null spermatocytes but normal in *Topbp1*$^{B5/B5}$ spermatocytes. Moreover, *Topbp1*$^{B5/B5}$ pachytene spermatocytes, but not *Setx* null spermatocytes, are able to reach the stage of crossover designation with MLH1 positive cells. Taken together, these observations suggest that *Topbp1*$^{B5/B5}$ pachytene spermatocytes progress further in pachynema when compared to *Setx* null spermatocytes and are consistent with a model in which a ATR-TOPBP1 control only specific(s) mode of SETX regulation[29,64].

The model involving SETX as a potential factor by which ATR controls silencing late in MSCI opens exciting directions to explore the interface of ATR-TOPBP1 with RNA processing. Given the established role for SETX in the resolution of R-loops[78], it is tempting to speculate that silencing defects in *Topbp1*$^{B5/B5}$ mutant may be related to aberrant accumulation of RNA-DNA hybrids that may affect removal of nascent mRNAs that is necessary for imposing silencing. In support of this model, R-loops affect chromatin architecture at promoters and interfere with the recruitment of transcription factors and chromatin remodelers, as observed in regions harboring CpG islands where R-loops prevent the action of DNA methyltransferases, thus preventing silencing[79]. Notably, highly transcribed genes, which tend to accumulate more R-loops[80], displayed increased silencing defects in the *Topbp1*$^{B5/B5}$ mutant.

While we have provided strong evidence to suggest a defect in later stages of MSCI as the cause of the cell death observed in *Topbp1*$^{B5/B5}$ spermatocytes, we cannot exclude the potential contribution of other defects, beyond silencing, to the loss of diplotene cells. The increased number of MLH1 foci suggested an altered recombination pattern, possibly impairing the ratios of class I and class II crossovers. The BRCT 5 domain of TOPBP1 interacts with the BLM helicase[27,59], which has been found to play a role in meiotic recombination in yeast and mice[81,82]. *Blm* CKO mice display severe defects in prophase I progression in spermatocytes, including, incorrect pairing and synapsis of homologs, and defective processing of recombination intermediates, leading to increased chiasmata[82]. These observations raise the possibility that impaired meiotic

progression and cell death in *Topbp1*$^{B5/B5}$ spermatocytes is a combination of defects in MSCI and recombination. *Topbp1*$^{B5/B5}$ spermatocytes do not progress beyond pachytene hence we were not able to visualize chiasmata and directly infer whether or not *Topbp1*$^{B5/B5}$ is defective in crossing over.

Our findings showing that TOPBP1 plays a specific role in silencing reinforcement after the first wave of MSCI are consistent with the recently proposed notion that the establishment and maintenance of MSCI is a dynamic process[17,64]. Also consistent with this notion is our recent finding showing that ATR signaling is itself also highly dynamic and constantly being cycled[64]. For example, using mice treated with the ATR inhibitor (ATRi) AZ20 for four hours, we found that such a short treatment is already sufficient to cause a complete loss of γH2AX, pMDC1 and SETX localization from the XY chromosomes[17,64]. Furthermore, germ cells subjected to ATRi for 24 hours showed complete recovery of γH2AX only three hours after release from ATRi treatment[17]. We propose that TOPBP1 acts on this phospho-cycle to ensure proper silencing reinforcement and maintenance, potentially by counteracting the engagement of anti-silencing factors that dynamically enter the sex body and need to be actively antagonized at the XY. Future work involving the characterization of possible unknown interactors of the BRCT domain 5 of TOPBP1, as well as functional dissection of ATR targets in MSCI, is essential to understand how TOPBP1 modulates the silencing machinery and shapes silencing dynamics.

In summary, our study presents a unique model for investigating the role of DDR factors in XY silencing. By allowing the uncoupling of MSCI progression from sex body formation, the *Topbp1*$^{B5/B5}$ mutant enables the study of MSCI dynamics during key stages late in pachynema. Notably, the inability of *Topbp1*$^{B5/B5}$ to sustain or reinforce silencing opens the possibility of uncovering new insights into the MSCI-dependent pachytene checkpoint.

STAR*Methods

Key resource table

Reagent type	Designation	Source or Reference	Identifiers	Additional information
Primer	p3xflag-TOPBP1-Flag-N-terminal-F	IDT	PCR primer	attcatcgatagatctgata ATGTCCAGAAAT GACAAAGA
Primer	p3xflag-TOPBP1-Flag-N-terminal-R	IDT	PCR primer	tagagtcgactggtaccgat tagTGTACTCTAG GTCGTT
Primer	hTopbp1_K1317A_R	IDT	Site-directed mutagenesis	tgccactgaggctaaatac gcctcgtttcgaagtggatg t
Primer	hTopbp1_K1317A_F	IDT	Site-directed mutagenesis	acatccacttcgaaacgag gcgtatttagcctcagtggc a
Primer	hTopbp1_K155A_F	IDT	Site-directed mutagenesis	caggtttgcagcaactaaat atgctttgctaccaacttctc ctgca
Primer	hTopbp1_K155A_R	IDT	Site-directed mutagenesis	tgcaggagaagttggtagc aaagcatatttagttgctgca aacctg
Primer	hTopbp1_K250A_R	IDT	Site-directed mutagenesis	tctcttggcacactcatacg cctgacctttggttcttgc
Primer	hTopbp1_K250A_F	IDT	Site-directed mutagenesis	gcaagaaccaaaaggtca ggcgtatgagtgtgccaag aga
Primer	musTopbp1_BRCT5-Fwd genotyping	IDT	PCR primer	tgcatttccattaaccaacct c
Primer	musTopbp1_BRCT5 Rev genotyping	IDT	PCR primer	ggtagagttcaaatgtgtgt catg
Antibody	phospho H2A.X (Ser139)	Millipore	Cat# 05-636;RRID:AB_309864	IF (meiotic spreads) 1:50000 IF 1:2000

Antibody	SCP3 antibody	Abcam	Cat# ab97672;RRID: AB_10678841	IF (meiotic spreads) 1:1000
Antibody	SYCP3	Lenzi et. al, 2005[83]	Custom	IF (meiotic spreads) 1:10000
Antibody	SCP1	Abcam	ab15090	IF (meiotic spreads) 1:1000
Antibody	Rad51	Millipore	PC130	IF (meiotic spreads) 1:1000
Antibody	ATR	Cell signaling	2790	IF (meiotic spreads) 1:1000
Antibody	TOPBP1	Danielsen et.al, 2008[84]	Custom	IF (meiotic spreads) 1: 500 Western blot 1:1000
Antibody	phospho-Chk1 (ser317)	Cell Signaling	12302	IF (meiotic spreads) 1: 100 Western blot 1:1000
Antibody	H1T	A gift from Dr. Mary Ann Handel[50]	Custom	IF (meiotic spreads) 1: 500
Antibody	HORMAD2	Wojtasz et. al, 2012[85]	Custom	IF (meiotic spreads) 1: 500
Antibody	HORMAD1	Wojtasz et. al, 2012[85]	Custom	IF (meiotic spreads) 1: 500
Antibody	phospho HORMAD2 (S271)	Wojtasz et. al, 2009	Custom	IF (meiotic spreads) 1: 500
Antibody	GAPDH	Thermo Fisher Scientific	AM4300	Western blot 1:5000
Antibody	β-Actin	Cell Signaling	4967	Western blot 1:5000
Antibody	phospho MDC1 (T4)	Abcam	Ab35967	IF (meiotic spreads) 1: 500
Antibody	SETX	Abcam	Ab220827	IF (meiotic spreads) 1: 100
Antibody	SETX	Novus	NBP1-94712SS	Western blot 1:1000

		Biologicals		
Antibody	MLH1	BD Biosciences	550838	IF (meiotic spreads) 1: 200
Antibody	MLH3	A gift from Dr. Paula Cohen[86]	Custom	IF (meiotic spreads) 1: 200
Antibody	CHK1	Santa Cruz	sc-8408	Western blot 1:1000
Antibody	CHK2	Millipore	05-649 (clone7)	Western blot 1:1000
Antibody	phospho CHK1 (S345)	Cell Signaling	2341	IF (meiotic spreads) 1: 200 Western blot 1:1000
Antibody	phospho RPA (S4/S8)	Bethyl	A300-245A,	Western blot 1:1000
Antibody	RPA (made against full length RPA2 expressed and purified in *E. Coli* and injected to rabbit)	N/A	Custom	Western blot 1:1000
Antibody	KAP1	Bethyl	a700-014-T	Western blot 1:1000
Antibody	phospho KAP1 (S824)	Bethyl	A300-767A-T	Western blot 1:1000
Antibody	53BP1	Cell signaling	4937	Western blot 1:1000
Antibody	53BP1	Novus Biologicals	NB100-304	IF (meiotic spreads) 1: 200
Antibody	BLM	Abcam	ab2179	Western blot 1:500
Antibody	Rad9	Bethyl	A300-890A-T	Western blot 1:1000
Antibody	BRCA1	Kakarougkas et. al, 2013[87]	Custom	IF (meiotic spreads) 1: 200
Antibody	BRCA1	Proteintech	22362-1-AP	Western blot 1:1000
Antibody	MDC1	Modzelewski et. al, 2015[88]	Custom	IF (meiotic spreads) 1: 200 IF

				1: 200
Antibody	RNA pol 2	Millipore	05-623	IF (meiotic spreads) 1: 2000
Antibody	phospho RNA pol 2 (Ser2)	Millipore	04-1571	IF (meiotic spreads) 1: 400
Antibody	phospho RNA pol 2 (Ser5)	Millipore	04-1572	IF (meiotic spreads) 1: 400
Antibody	H3K9ac	Abclonal	A7255	IF (meiotic spreads) 1: 200
Antibody	H3K9me3	Active Motif	39766	IF (meiotic spreads) 1: 200
Antibody	H3K4me1	Abclonal	A2355	IF (meiotic spreads) 1: 200
Antibody	CHD4	Abclonal	A10557	IF (meiotic spreads) 1: 200
Antibody	Sumo_2/3	Proteintech	G67154-1-1g	IF (meiotic spreads) 1: 200
Antibody	USP7	Proteintech	66514-1-Ig	IF (meiotic spreads) 1: 200
Antibody	H3K27ac	Active Motif	39134	IF (meiotic spreads) 1: 200
Antibody	H3K36ac	Active Motif	61102	IF (meiotic spreads) 1: 200
Antibody	H3K4me3	Active Motif	39160	IF (meiotic spreads) 1: 200
Antibody	H4K16ac	Abclonal	A5280	IF (meiotic spreads) 1: 200
Antibody	H4c	Millipore	06-598	IF (meiotic spreads) 1: 200
Antibody	H2AK199ub	Abcam	Ab193203	IF (meiotic spreads) 1: 200
Antibody	Goat anti-rabbit IgG (H + L) highly	Thermo Fisher Scientific	A-11034	IF (meiotic spreads) 1: 1000

	cross-adsorbed secondary antibody, Alexa Fluor 488			
Antibody	Goat anti-mouse IgG (H + L) antibody, Alexa Fluor 488 conjugated	Thermo Fisher Scientific	A-11017	IF (meiotic spreads) 1: 1000
Antibody	Goat anti-rabbit IgG (H + L) antibody, Alexa Fluor 594 conjugated	Thermo Fisher Scientific	A-11012	IF (meiotic spreads) 1: 1000
Antibody	Goat anti-mouse IgG (H + L) highly cross-adsorbed secondary antibody, Alexa Fluor Plus 594	Thermo Fisher Scientific	A32742	IF (meiotic spreads) 1: 1000
Antibody	Goat anti-guinea pig IgG (H + L) highly cross-adsorbed secondary antibody, Alexa Fluor 647	Thermo Fisher Scientific	A-21450	IF (meiotic spreads) 1: 1000
Commercial assay or kit	ApopTag Plus Peroxidase In Situ Apoptosis Kit	Millipore	S7101	N/A
Software, algorithm	GraphPad Prism 9	GraphPad Prism	RRID:SCR_002798	N/A
Software	Cellranger v7.0.0	10X Genomics	https://support.10xgenomics.com/single-cell-gene-expression/software/downloads/3.1	N/A

Software	R v4.2.1	R Foundation	RRID:SCR_001905	N/A
Software	Seurat v4.3.0	Hao et. al, 2013[89]	RRID:SCR_007322	N/A
Software	sva v3.44.0	Leek et. al, 2023[90]	RRID:SCR_012836	N/A
Software	SingleR v1.10.0	Aran et. al, 2019[91]	RRID:SCR_023120	N/A
Software	Reshape2 v1.4.4	Wickham, 2007[92]	RRID:SCR_022679	N/A
Software	biomaRt v2.52.0	Durinck et. al, 2009[93]	RRID:SCR_019214	N/A
Software	ggpubr v0.5.0	Kassambara, 2009[94]	RRID:SCR_021139	N/A
Software	Tidyverse v1.3.2	Wickham et. al, 2019[95]	RRID:SCR_019186	N/A
Software	ggnewscale v0.4.8	Campitelli	https://eliocamp.github.io/ggnewscale/index.html	N/A
Software	Harmony v0.1.1	Korsunsky et.	RRID:SCR_02	N/A

		al, 2019[96]	2206	
Software	Org.Mm.eg.db v3.15.0	Carlson, 2019[97]	RRID:SCR_023488	N/A
Software	Corrplot v0.92	Wei et. al, 2017[98]	RRID:SCR_023081	N/A
Software	SeuratWrappers v0.3.1	Satija Lab	RRID:SCR_022555	N/A
Software	gghalves v0.1.4	Tiedemann	https://github.com/erocoar/gghalves	N/A

Resource availability

Lead contact

Further information and requests for resources and data should be directed to and will be fulfilled by the lead contact, Marcus Smolka (email: mbs266@cornell.edu).

Materials availability

This study generated a unique antibody, RPA.

Mice, genotyping and treatment of mice with IR

All mice used in this work were handled following federal and institutional guidelines under a protocol approved by the Institutional Animal Care and Use Committee (IACUC) at Cornell University. CRISPR/Cas9 editing was used to engender the *Topbp1B5* allele and performed by the Cornell Mouse Modification core facility. To this end, the online tools CRISPR gold and ChopChop were used to generate high quality (guide score >9) CRISPR guide RNAs targeting the intronic sequences neighboring the genomic sequence of *Mus musculus topbp1* exon 13. The

CRISPR crRNAs (purchased from IDT) harboring the sequences ccaactcaggtcggccgctcttg and cctcgattagtcctcaaggcgag (PAM sites are underlined), both targeting the reverse strand, the repair template (below), and CAS9 RNA were injected on embryos from super ovulated, plugged C57BL/6J female mice crossed to C57BL/6J stud males. 2-cell stage embryos were then implanted on pseudo pregnant females and pups were genotyped after one week old.

Repair template:

acagcagggcttctctgtgtaaccctctctccgtagaccagtttggccttgatcgaactcaggtcggccgctcttgcctctagagtcctgggat
taaaggcgtgcactgccaccacccagagtatgtttctctgacattaaccatgctattattttttaaaatgagctaattgtgtgttcatttgctttattt
ccatgtaaaattttagTGTTCAAGAATTCTTTGTTGACGAAGCCAATGCAGAGGAAGGCATGCT
CGCCAGCACACATCTTATAGTGGAGGAACCGACTGGTTCCGAATACGAAGCTGCAG
AGGAATGGAGTTTGCCGGCAGTTAACATTTCATGGCTCTTAGAAACTGCGGAAATCG
GGGAGGAAGCAGATGAAAACCATTTTCTGGTTGACAACGCACCTAAACAAGgttagaagt
ccttgtttttttttatgtattttacaacttgatggtttctgaaatagggatgttccagtacttgctttaaaacatttgtatgaccctaacctcagtcagtg
gtgcttacttcagaacccctgagtgaaacacggaaagcagatcaatgaagaagcgcatcagggtcaacggtcgattagtcctcaaggcga
gtgacgagaaggtgacccccga atggctgttagaagcagtttttata (purchased from IDT as a G-block)

Intronic sequence is shown in lower case, exon 13 sequence is shown in capital letters; underline represents the mutated residues, pink represents the mutated PAM residues, in orange is shown the guide RNA sequences and in red, the targeted amino acid sequences. Of note, although this repair template encodes for 11 amino acid changes, only 8 were successfully inserted into the mouse topbp1 exon 13 locus. For mice genotyping, the following primers were used 5'-tgcatttccattaaccaacctc-3' and 5'- ggtagagttcaaatgtgtgtcatg-3' (also shown at key resources table). For irradiation, *Topbp1*$^{+/+}$ and *Topbp1*$^{B5/B5}$ mice were placed in a 137 Cesium-sealed source irradiator (J.L. Shepherd and Associates) with a rotating turntable and irradiated with 7 Gy IR.

MEFs and cell survival assays

MEFs were prepared from E13.5 mouse embryos as previously described [99]. Briefly, embryos were dissected and mechanically disrupted using pipette aspiration until homogenous. Cells were allowed to settle, and the supernatant was transferred into Dulbecco's modified medium supplemented with 10% fetal bovine serum, 1% penicillin/streptomycin and 1% nonessential amino acids. Following four days of growth, cells were then immortalized by transduction with a large-T antigen lentivirus. Subsequently, cells were selected with 10 µg/mL puromycin.

For colony survival assays, 500 cells were seeded per 10 cm dish, allowed to adhere for 24h and treated with Phleomycin or Hydroxyurea for 24h (drug concentrations are displayed on figure 2A-D and Supplemental Figure 2). In the following day, cells were released and let to form colonies for 10-15 days. Cells were then washed once with PBS, fixed in 100% methanol for 1h, stained with 0.1% crystal violet (MP Biomedicals, 152511) solution overnight, and then washed with distilled water before imaging and counting.

For accessing DDR and checkpoint responses via western blot, 2 x 10^6 cells were seeded on a 60 cm dish, allowed to adhere for 24h, and treated with Phleomycin or Hydroxyurea for 3h (drug concentrations are displayed on Figure 2).

Cell culture

HEK-293T cells were cultured in Dulbecco's modified medium supplemented with 10% fetal calf serum, 1% penicillin/streptomycin and 1% nonessential amino acids. Immortalized MEFs were cultured in Dulbecco's modified medium supplemented with 10% fetal calf serum, 1% penicillin/streptomycin, 1% nonessential amino acids, and 1% glutamine supplementation. All cells were kept at 37°C and 5% CO_2. All the cell lines were regularly tested for mycoplasma contamination with the Universal Mycoplasma Detection Kit (ATCC). HEK-293T cells were transfected using homemade polyethylenimine (Polysciences, Inc.). 36h after transfection, cells were treated with 1mM HU (Hydroxyurea) and then harvested for immunoprecipitation experiments.

Plasmids

The full-length TOPBP1 CDS was cloned on a p3xflag vector (Milipore/Sigma E7658) using Gibson assembly (NEB) following the manufacturer's instructions. The p3xflag-TOPBP1 was used as a template to generate p3xflag-TOPBP-K155A, p3xflag-TOPBP-K250A, p3xflag-TOPBP-K704A, p3xflag-TOPBP-K1317A through site-directed mutagenesis using prime STAR master mix (Takara) and Gibson assembly to generate p3xflag-TOPBP-KE, using the following G-block (IDT) containing the 8 charge-reversal point mutations at the BRCT 5 domain of TOPBP1:

AACGAATCCAATGCAGAAGAAGGCATGTTTGCCAGTACTCATCTTATACTGGAAGA ACGTGGTGGCTCTGAATATGAAGCTGCAAAGAAGTGGAATTTACCTGCCGTTACTAT AGCTTGGCTGTTGGAGACTGCTAGAACGGGAGAAGA.

All primers used for the cloning are shown in the key resources table.

Immunoblotting

Cells were harvested and lysed in modified RIPA buffer (50 mM Tris–HCl, pH7.5, 150 mM NaCl, 1% Tergitol, 0.25% sodium deoxycholate, 5 mM ethylenediaminetetraacetic acid (EDTA)) supplemented with complete EDTA-free protease inhibitor cocktail (Roche), 1 mM phenylmethylsulfonyl fluoride (PMSF) and 5 mM NaF. Whole cell lysates, after sonication, were cleared by 15 min centrifugation at 17,000 xg at 4◦C. Twenty micrograms of protein extract were mixed with 3X sodium dodecyl sulfate sample buffer and resolved by SDS-PAGE. Gels were transferred on polyvinylidene difluoride membranes and immunoblotted using standard procedures. Western blot signal was acquired with a Chemidoc Imaging System (BioRad). Antibody information is provided in the key resources table.

Immunofluorescence

MEFs were grown on coverslips and then submitted to IR, 5 gy and allowed to recover for 1.5h at 37°C and 5% CO_2. Cells were then fixed using 3.7% formaldehyde in phosphate-buffered saline (PBS) for 10 min at room temperature (RT). Fixed cells were then washed 3x with PBS, permeabilized for 5 min with 0.2% Triton X-100/PBS at RT and blocked in 10% bovine serum albumin/PBS for 20 min at RT. Coverslips were incubated first with primary antibodies for 2h at RT, followed by three washes with PBS, and then for 1 hour with relative secondary antibodies. After incubation with secondary antibodies, coverslips were washed three times with PBS and then mounted on glass microscope slides using DAPI–Vectashield mounting medium (Vector Laboratories). Slides were imaged on a Leica DMi8 Microscope with a Leica DFC9000 GTC camera using the LAS X (Leica Application Suite X) software with a 100x objective. For micronuclei scoring, ∼150–200 cells/replicate were counted. The two-tailed Student's t-test was used for statistical analysis. Antibody information is provided in the key resources table.

Meiotic Spreads

Meiotic surface spreads were performed from 8- to 12-week-old mice as described by Kolas et al.,[100] .Briefly, decapsulated testis from mice were incubated on ice in a hypotonic extraction buffer for 45 min. Tubules were then minced into single- cell suspension in 100 mM sucrose, and cells were spread on slides coated with 1% PFA with 0.15% TritionX- 100 and incubated in a humidifying chamber for 4h. For immunostaining, slides were blocked using 10% goat serum and 3% BSA, followed by incubation overnight with primary antibody (listed in the STAR methods) at 4°C in a humidifying chamber. Secondary antibodies were incubated at 37°C for 2h in the dark, and slides were then cover-slipped using antifade mounting medium (2.3% DABCO, 20 mM Tris pH 8.0, 8 µg DAPI in 90% glycerol). Slides were imaged on a Leica DMi8 Microscope with a Leica DFC9000 GTC camera using the LAS X (Leica Application Suite X) software. For every condition, a minimum of 50 images from at least two independent mice were acquired. To quantify fluorescence intensity, the LAS X software quantification tool was used as previously described[64]. Antibody information is provided in the key resources table.

3D-Structured Illumination super resolution Microscope (3D-SIM)

Higher resolution images were acquired using an ELYRA 3D-Structured Illumination Super Resolution Microscopy (3D-SIM) from Carl Zeiss with ZEN Black software (Carl Zeiss AG, Oberkochen, Germany). Images are shown as maximum intensity projections of z stack images. To reconstruct high-resolution images, raw images were computationally processed by ZEN Black. The brightness and contrast of images were adjusted using ImageJ (National Institutes of Health, USA). Antibody information is provided in the key resources table.

Fertility assays

For fertility testing, 8 weeks old *Topbp1*$^{B5/B5}$ females and C57BL/6 males or C57BL/6 females and *Topbp1*$^{B5/B5}$ males were singly housed, where pregnancies were monitored for a period of one month. Viable pups were counted on the first day of life. For *Topbp1*$^{B5/B5}$ males, breeding cages remained active for a period of six months and at no time pregnant females nor birth of pups were detected. No noticeable defects were found on fertility of Topbp*1*$^{B5/+}$, males or females (data not shown).

TUNEL

TUNEL assay was conducted using the Apoptag kit (EMD Millipore) following the manufacturer's instructions. The data were quantified in Image Scope by counting the number of positive cells per tubule for 100 tubules of each genotype, 3 mice each. Statistical differences between *Topbp1*$^{+/+}$ and *Topbp1*$^{B5/B5}$ were analyzed using Welch's unpaired t- test in GraphPad.

Hematoxylin and eosin staining

Adult testes - from 12 weeks old mice - were dissected and incubated in Bouin's fixative overnight, washed during 30 min each in 30%, then 50% and then 70% ethanol. The 70% ethanol wash was repeated 3 times more. Testes were then embedded in paraffin. 5 µm sections were mounted on slides. After rehydration in Safe Clear Xylene Substitute followed by decreasing amounts of ethanol, slides were stained with hematoxylin followed by eosin. The slides were then gradually dehydrated by incubation in increasing concentrations of ethanol before mounting using toluene mounting medium.

Epididymal sperm counts

Caudal and epididymides from 8- to 12-week-old mice were minced with fine forceps at 37°C in a Petri dish containing Dulbecco's modified medium supplemented with 10% fetal calf serum, 1% penicillin/streptomycin, 4% BSA, and 1% nonessential amino acids. Samples were then incubated at 37°C for 30 min allowing sperm to swim out into the media, then fixed in 10% neutral-buffered formalin (1:25 dilution). Sperm cells were counted using a hemocytometer and analyzed statistically using the two-tailed Student's t-test between *Topbp1*$^{+/+}$ and *Topbp1*$^{B5/B5}$.

Enrichment of testes phosphopeptides and TMT labeling

The enrichment of testes phosphopeptides and TMT labeling were done as described previously[64]. Briefly, whole decapsulated testes were collected from 8- to 12-week-old mice after which tissue was subject to lysis, protein quantification and normalization, denaturation, alkylation, precipitation, digestion, and solid-phase extraction (SPE) C18 cartridge clean up as described by Sims et. al[64]. Lyophilized tryptic peptides were then subject to phosphopeptide enrichment using a High-Select Fe-NTA Phosphopeptide Enrichment Kit according to the manufacturer's protocol (Cat# A32992, Thermo Scientific). Phosphopeptide samples were dried in silanized glass shell vials, resuspended in 50 mM HEPES, and labeled with 100 µg of TMT sixplex Isobaric Label

Reagents (Thermo Scientific) using 3 TMT channels for each condition (*Topbp1*$^{+/+}$ and *Topbp1*$^{B5/B5}$). The TMT-labeling reaction was done at room temperature for 1h and quenched with 5% hydroxylamine for 15 minutes. After quenching, TMT-labeled peptides from all six channels were pooled, acidified with 0.1% TFA, and desalted using a SPE 1cc C18 cartridge (Sep-Pak C18 cc vac cartridge, 50 mg Sorbent, WAT054955, Waters). Bound TMT-labeled phosphopeptides were eluted with 80% acetonitrile, 0.1% acetic acid in water before being dried via vacuum concentrator.

Mass spectrometric analysis of TMT-labeled phosphopeptides

The dried TMT-labeled phosphopeptides were prefractionated using offline HILIC HPLC prior to being analyzed by mass-spectrometry as described by Sims et. al[64]. The LC-MS/MS was performed on an UltiMate 3000 RSLC nano chromatographic system coupled to a Q-Exactive HF mass spectrometer (Thermo Fisher Scientific). The chromatographic separation was achieved via a 35cm-long 100 µm inner diameter column packed in-house with 3 µm C18 reversed-phase resin (Reprosil Pur C18AQ 3 µm). The Q-Exactive HF was operated in data-dependent mode with survey scans acquired in the Orbitrap mass analyzer over the range of 380–1800 m/z with a mass resolution of 120,000. MS/MS spectra were performed after selecting the top 7 most abundant +2, +3, or +4 ions and a precursor isolation window of 0.7 m/z. Selected ions were fragmented by Higher-energy Collisional Dissociation (HCD) with normalized collision energies of 28, with fragment mass spectra acquired in the Orbitrap mass analyzer with a monitored first mass of 100 m/z, mass resolution of 15,000, AGC target set to 1×10^5, and maximum injection time set to 100 ms. A dynamic exclusion window of 30 seconds was specified.

Phosphoproteomic data analysis

The Trans Proteomic Pipeline (TPP) version 6.0.0 was used for phosphopeptide identification and quantification. MS data were converted to mzXML using msConvert as packaged with the TPP, after which spectral data files were searched using the Comet search engine (v2021 rev 1)[101]. Peptide identifications were validated using PeptideProphet, phosphorylation site localization was performed using PTM Prophet, and TMT channel quantification was performed using Libra. Results from Libra were exported as tab-delimited files for further processing via R scripts as previously described[64]. The mass spectrometry phosphoproteomics data have been deposited to

the ProteomeXchange Consortium via the PRIDE [1] partner repository with the dataset identifier PXD042199.

Immunoprecipitation

The immunoprecipitation (IP) experiments were performed as described by Liu et. al[22]. Briefly, cell pellets were lysed in 50 mM Tris-HCl, pH 7.5, 150 mM NaCl, 1% tergitol, 0.25% sodium deoxycholate, and 5 mM EDTA, supplemented with EDTA-free protease inhibitor cocktail, 5 mM sodium fluoride, 10 mM β-glycerolphosphate, 1 mM PMSF, and 0.4 mM sodium orthovanadate. The protein extracts were cleared by 10-min centrifugation and then were incubated with anti-FLAG agarose beads (Sigma-Aldrich) for 16h at 4°C. The beads were then washed four times with the same buffer used for IP and then eluted using three resin volumes of the elution buffer (100 mM Tris-HCl, pH 8.0, and 1% SDS, and 1 mM DTT).

Mass spectrometric analysis of immunoprecipitates

HEK-293T cells were grown in stable isotope labeling with amino acids in cell culture (SILAC) as previously described[22] and transfected as described above. Cells were treated with 1 mM HU for 16h before harvesting. Flag-TOPBP1 was immunoprecipitated using anti-FLAG agarose beads. Immunoprecipitates were then prepared for mass spectrometry analysis by reduction, alkylation, precipitation, and digestion by trypsin. The peptides were desalted, dried, and then fractionated by hydrophilic interaction chromatography as previously described[22]. Fractions were dried and analyzed by liquid chromatography–tandem mass spectrometry using a mass spectrometer (Q-Exactive HF Orbitrap; Thermo Fisher Scientific). The capillary column was 35 cm long with a 100-µm inner diameter, packed in-house with 3 µm C18 reversed-phase resin (Reprosil Pur C18AQ 3 µm). Peptides were separated over an 70-minute linear gradient of six to 40% acetonitrile in 0.1% formic acid at a flow rate of 300 nl/min as described previously[102]. Xcalibur 2.2 software (Thermo Fischer Scientific) was used for the data acquisition, and The Q-Exactive HF was operated in data-dependent mode with survey scans acquired in the Orbitrap mass analyzer over the range of 380–1800 m/z with a mass resolution of 120,000. The maximum ion injection time for the survey scan was 100 ms with a 3e6 automatic gain-control target ion. Tandem mass spectrometry spectra were performed by selecting up to the 20 most abundant ions with a charge state of 2, 3, or 4 and with an isolation window of 1.2 m/z. Selected ions were

fragmented by higher energy collisional dissociation with a normalized collision energy of 28, and the tandem mass spectra was acquired in the Orbitrap mass analyzer with a mass resolution of 17,500 (at m/z 200). The Trans Proteomic Pipeline (TPP) version 6.0.0 was used for peptide identification and SILAC quantification. MS data were converted to mzXML using msConvert as packaged with the TPP, after which spectral data files were searched using the Comet search engine (v2021 rev 1)[101]. The following parameters were used in the database search: semitryptic requirement, a mass accuracy of 15 ppm for the precursor ions, a differential modification of 8.0142 D for lysine and 10.00827 D for arginine, and a static mass modification of 57.021465 D for alkylated cysteine residues. Peptide identifications were validated using PeptideProphet and SILAC quantification was performed using XPRESS as described previously[102]. The mass spectrometry data have been deposited to the ProteomeXchange Consortium via the PRIDE [1] partner repository with the dataset identifier PXD042199.

Total germ cells preparation

Mice testis were collected from 8- to 12-week-old mice (n = 5 mice, 10 testis for *Topbp1*$^{+/+}$, and n = 20-30 mice, 40-60 testis for *Topbp1*$^{B5/B5}$), and dissociated using standard protocols for germ cell extraction[73]. Briefly, decapsulated testes were held in 10 ml of preheated (35°C) DMEM-F12 buffer containing 2 mg of Collagenase 1A and DNAse 7 mg/ml, on a 50 ml conical tube. The collagenase digestion was performed at a 35°C shaker water-bath, 150 rpm during 5 min. The collagenase digestion was stopped by the addition of 40 ml of DMEM-F12 and the tubules were let to decantate for 1 min. The supernatant was removed and added another 40 ml of DMEM-F12 to further wash the residual collagenase and remove somatic and excessive sperm cells. Next, the tubules were digested using 10 ml of DMEM-F12 buffer containing 5 mg of trypsin (Thermo Fisher 27250018) on a 50 ml conical tube and the reaction was carried out on a 35°C shaker water-bath, 150 rpm during 5 min. Digested tubules were strained on a 100 μm strainer containing 3 ml of FBS (100% Fetal Bovine Serum, heat inactivated, Sigma F4135-500mL). Total germ cells were centrifuged at 300 xg for 5 min, 4°C and checked for single cells and viability.

Flow cytometry analysis

Total germ cell extracts were stained with Vybrant dye cycle (VDG) (Invitrogen) 100 μM for 30 min at room temperature, kept on dark, and rocking. After staining, cells were sorted as previously

described[103] aiming to enrich for spermatocytes, and using the Sony MA900 fluorescent activated cell sorter (FACS), tuned to emit at 488 nm and with a 100 μm nozzle. Laser power was set to collect VDG-emitted fluorescence in FL1. Sorted cells were collected on 1.5 ml tubes containing 0.5 ml of DMEM-F12 buffer + 10% FBS. The FACS was done at the Flow Cytometry Facility - Cornell University.

Single-Cell RNA sequencing

Flow sorted cells were submitted to the Cornell DNA Sequencing Core Facility and processed on the 10X Genomics Chromium System targeting 5000–7000 cells per sample as described previously[73] using the 10X Genomics Chromium Single Cell 3′ RNA-seq v2 kit to generate the sequencing libraries, which were then tested for quality control on an ABI DNA Fragment Analyzer and ran on a NextSeq platform with 150 base-pair reads. The sequencing was carried out to an average depth of 98M reads (range 77M-124M); on average, 91% of reads (range 89%-92%) and then mapped to the reference genome.

Single-cell RNA sequencing data analysis

Count matrices were generated for each sample using the Cell Ranger counts function and then imported into Seurat and integrated. Cells were filtered based on gene number, UMI, counts, and mitochondrial percentage. Cells with less than 500 genes, less than 1000 UMIs, or more than 5% of mitochondrial reads were excluded from further analysis (Supplemental Figure 29). Raw counts were normalized using Seurat NormalizeData using default parameters and the top 4000 variable features were identified using the FindVariableFeatures function using ExpMean for the mean function and LogVMR for the dispersion function. Principal components were calculated from variable genes and used with Harmony to correct for batch effect. Harmony embeddings dimensions 1-20 were used for a Shared Nearest Neighbor graph with k=30, unsupervised clustering with a resolution of 4, and Uniform Manifold Approximation and Projection (UMAP) analysis. Cell types were manually identified by use of marker genes, and the SingleR package was used to confirm cell identity. Chromosome X/autosome 9 ratios were calculated by taking the mean gene expression of all genes on chromosome 9 or X for a cell and dividing it by the mean gene expression for all autosomal genes in a cell. Ratios were visualized using ggplot and the introdataviz package geom_split_violin function. The single cell heatmap was generated using the

DoHeatmap function. The clustered analysis of the X-linked genes shown in Figure 7A, was done by splitting the detected 233 X-linked genes into 3 distinct categories based on the difference of RNA level between the spermatocyte stages and normalized by pre-leptotene: reduced silencing (> 1), unaltered silencing (≥ -1 or ≤ 1), or increased silencing (< -1). To further split the X-linked genes into 3 categories based on the severity of the silencing defect (detected at spermatocyte 3 stage) in *Topbp1*$^{B5/B5}$: no defect (13 genes), mild (45 genes) or strong defect (170 genes), the difference in expression between SP3 genes from *Topbp1*$^{+/+}$ or from *Topbp1*$^{B5/B5}$ was calculated. The categories were defined as: Strong > 2.5, Mild ≥ 1 or ≤ 2.5 and no defect <1. The Single-cell RNAseq data generated in this study have been deposited in the NCBI GEO database under accession number GSE232588.

Data and code availability

All data and original codes reported in this work, and any additional information required will be shared by the lead contact upon request.

Acknowledgments

We thank the members of Cohen lab, Weiss lab, Grimson lab and Smolka lab for comments and suggestions. We thank Dr. Fenghua Hu and Dr. Tony Bretscher for the use of the microscopes and Beatriz Almeida for technical assistance. We thank Dr. Lydia Tesfa and the BRC Flow Cytometry Facility (RRID:SCR_021740) for training and assistance with FACS at the Cornell Institute of Biotechnology, Peter Schweitzer and the BRC Genomics Facility (RRID:SCR_021727) at the Cornell Institute of Biotechnology for sequencing experiments, Johana M. de la Cruz and the BRC Imaging Facility (RRID:SCR_021741) at the Cornell Institute of Biotechnology for training and assistance with the Elyra Super Resolution Microscope and the 3D-SIM imaging. We thank Marco Hiler and the BMS and Stem Cell Pathology Unit at the Cornell Veterinary Research Tower for training and assistance with imaging histological sections using ScanScope. We thank Dr. John Schimenti, Dr. Robert Munroe, Mr. Christian Abratte, and Cornell's Stem Cell and Transgenic Core Facility for generating the *Topbp1*$^{B5/B5}$ mouse. We thank Dr. Paula Cohen for the MLH3 antibody, and Dr. Mary Ann Handel for the H1T antibody.

Author contributions

M.B.S, C.F.R.A and J.R.S. conceived the project. M.B.S and C.F.R.A wrote the paper. C.F.R.A and J.R.S contributed equally with conceptualization, data curation and formal analysis. C.F.R.A, J.R.S and E.A.F. performed experiments. A.D and A.G contributed with data curation and formal analysis. W.C and J.B contributed with data analysis. M.B.S, C.F.R.A, R.W. and P.E.C, contributed with funding acquisition. R.F. contributed with resources.

Declaration of interests

No competing interests declared.

Inclusion and diversity

We support inclusive, diverse, and equitable conduct of research.

Funding

This work was supported by Eunice Kennedy Shriver National Institute of Child Health and Human Development (R01-HD095296) to M.B.S and R.W, National Institute of Health – General Medicine (R35-GM141159) to M.B.S, National Institute of Health (R01HD041012) to P.E.C, the Eunice Kennedy Shriver National Institute of Child Health and Human Development (P50HD104454) to A.G., the Spanish Agencia Estatal de Investigación [PID2019-109222RB-I00/AEI/10.13039/501100011033]; European Union Regional Funds (FEDER) to R. F., and 2022 CVG Scholar Award from the Center of Vertebrates Genomics and the 2022 ASCB International training Scholarship to C.F.R.A.

References

1. Subramanian, V.V., and Hochwagen, A. (2014). The meiotic checkpoint network: step-by-step through meiotic prophase. Cold Spring Harb. Perspect. Biol. *6*, a016675.

2. Handel, M.A., and Schimenti, J.C. (2010). Genetics of mammalian meiosis: Regulation, dynamics and impact on fertility. Nature Reviews Genetics *11*, 124–136. 10.1038/nrg2723.

3. Keeney, S., Giroux, C.N., and Kleckner, N. (1997). Meiosis-specific DNA double-strand breaks are catalyzed by Spo11, a member of a widely conserved protein family. Cell *88*. 10.1016/S0092-8674(00)81876-0.

4. Joshi, N., Brown, M.S., Bishop, D.K., and Börner, G.V. (2015). Gradual Implementation of the Meiotic Recombination Program via Checkpoint Pathways Controlled by Global DSB Levels. Mol. Cell *57*. 10.1016/j.molcel.2014.12.027.

5. Pereira, C., Smolka, M.B., Weiss, R.S., and Brieño-Enríquez, M.A. (2020). ATR signaling in mammalian meiosis: From upstream scaffolds to downstream signaling. Environmental and Molecular Mutagenesis *61*, 752–766. 10.1002/em.22401.

6. Gray, S., and Cohen, P.E. (2016). Control of Meiotic Crossovers: From Double-Strand Break Formation to Designation. Annu. Rev. Genet. *50*, 175–210.

7. Burgoyne, P.S., Mahadevaiah, S.K., and Turner, J.M.A. (2009). The consequences of asynapsis for mammalian meiosis. Nature Reviews Genetics *10*. 10.1038/nrg2505.

8. Turner, J.M.A., Mahadevaiah, S.K., Ellis, P.J.I., Mitchell, M.J., and Burgoyne, P.S. (2006). Pachytene asynapsis drives meiotic sex chromosome inactivation and leads to substantial postmeiotic repression in spermatids. Dev. Cell. 10.1016/j.devcel.2006.02.009.

9. Turner, J.M.A. (2015). Meiotic Silencing in Mammals. Annu. Rev. Genet. *49*. 10.1146/annurev-genet-112414-055145.

10. Abe, H., Alavattam, K.G., Hu, Y.C., Pang, Q., Andreassen, P.R., Hegde, R.S., and Namekawa, S.H. (2020). The Initiation of Meiotic Sex Chromosome Inactivation Sequesters DNA Damage Signaling from Autosomes in Mouse Spermatogenesis. Curr. Biol. *30*, 408-420.e5.

11. Turner, J.M.A. (2007). Meiotic sex chromosome inactivation. Development *134*, 1823–1831.

12. Alavattam, K.G., Abe, H., Sakashita, A., and Namekawa, S.H. (2018). Chromosome spread analyses of meiotic sex chromosome inactivation. In Methods in Molecular Biology (Humana Press Inc.), pp. 113–129.

13. Royo, H., Polikiewicz, G., Mahadevaiah, S.K., Prosser, H., Mitchell, M., Bradley, A., De Rooij, D.G., Burgoyne, P.S., and Turner, J.M.A. (2010). Evidence that meiotic sex chromosome inactivation is essential for male fertility. Curr. Biol. *20*, 2117–2123.

14. Vernet, N., Mahadevaiah, S.K., de Rooij, D.G., Burgoyne, P.S., and Ellis, P.J.I. (2016). Zfy genes are required for efficient meiotic sex chromosome inactivation (MSCI) in spermatocytes. Hum. Mol. Genet. *25*, 5300–5310.

15. Pacheco, S., Maldonado-Linares, A., Marcet-Ortega, M., Rojas, C., Martínez-Marchal, A., Fuentes-

Lazaro, J., Lange, J., Jasin, M., Keeney, S., Fernández-Capetillo, O., et al. (2018). ATR is required to complete meiotic recombination in mice. Nat. Commun. *9*. 10.1038/s41467-018-04851-z.

16. Royo, H., Prosser, H., Ruzankina, Y., Mahadevaiah, S.K., Cloutier, J.M., Baumann, M., Fukuda, T., Höög, C., Tóth, A., de Rooij, D.G., et al. (2013). ATR acts stage specifically to regulate multiple aspects of mammalian meiotic silencing. Genes and Development *27*. 10.1101/gad.219477.113.

17. Abe, H., Yeh, Y.-H., Munakata, Y., Ishiguro, K.-I., Andreassen, P.R., and Namekawa, S.H. (2022). Active DNA damage response signaling initiates and maintains meiotic sex chromosome inactivation. Nat. Commun. *13*, 7212.

18. Widger, A., Mahadevaiah, S.K., Lange, J., Elinati, E., Zohren, J., Hirota, T., Pacheco, S., Maldonado-Linares, A., Stanzione, M., Ojarikre, O., et al. (2018). ATR is a multifunctional regulator of male mouse meiosis. Nat. Commun. *9*. 10.1038/s41467-018-04850-0.

19. Cimprich, K.A., and Cortez, D. (2008). ATR: An essential regulator of genome integrity. Nature Reviews Molecular Cell Biology *9*. 10.1038/nrm2450.

20. Liu, Y., and Smolka, M.B. (2016). TOPBP1 takes RADical command in recombinational DNA repair. J. Exp. Med. *213*. 10.1084/jem.2132oia2.

21. Mordes, D.A., Glick, G.G., Zhao, R., and Cortez, D. (2008). TopBP1 activates ATR through ATRIP and a PIKK regulatory domain. Genes and Development *22*, 1478–1489.

22. Liu, Y., Cussiol, J.R., Dibitetto, D., Sims, J.R., Twayana, S., Weiss, R.S., Freire, R., Marini, F., Pellicioli, A., and Smolka, M.B. (2017). TOPBP1Dpb11 plays a conserved role in homologous recombination DNA repair through the coordinated recruitment of 53BP1Rad9. J. Cell Biol. *216*, 623–639.

23. Leimbacher, P.A., Jones, S.E., Shorrocks, A.M.K., de Marco Zompit, M., Day, M., Blaauwendraad, J., Bundschuh, D., Bonham, S., Fischer, R., Fink, D., et al. (2019). MDC1 Interacts with TOPBP1 to Maintain Chromosomal Stability during Mitosis. Mol. Cell *74*, 571-583.e8.

24. Cescutti, R., Negrini, S., Kohzaki, M., and Halazonetis, T.D. (2010). TopBP1 functions with 53BP1 in the G1 DNA damage checkpoint. EMBO J. *29*, 3723–3732.

25. Leung, C.C.Y., Gong, Z., Chen, J., and Glover, J.N.M. (2011). Molecular basis of BACH1/FANCJ recognition by TopBP1 in DNA replication checkpoint control. J. Biol. Chem. *286*, 4292–4301.

26. Delacroix, S., Wagner, J.M., Kobayashi, M., Yamamoto, K.I., and Karnitz, L.M. (2007). The Rad9-Hus1-Rad1 (9-1-1) clamp activates checkpoint signaling via TopBP1. Genes and Development *21*, 1472–1477.

27. Blackford, A.N., Nieminuszczy, J., Schwab, R.A., Galanty, Y., Jackson, S.P., and Niedzwiedz, W. (2015). TopBP1 Interacts with BLM to Maintain Genome Stability but Is Dispensable for Preventing BLM Degradation. Mol. Cell *57*, 1133–1141.

28. Bigot, N., Day, M., Baldock, R.A., Watts, F.Z., Oliver, A.W., and Pearl, L.H. (2019). Phosphorylation-mediated interactions with topbp1 couple 53bp1 and 9-1-1 to control the g1 DNA damage checkpoint. Elife *8*, 1–28.

29. Pereira, C., Arroyo-Martinez, G.A., Guo, M.Z., Downey, M.S., Kelly, E.R., Grive, K.J., Mahadevaiah, S.K., Sims, J.R., Faca, V.M., Tsai, C., et al. (2022). Multiple 9-1-1 complexes promote homolog synapsis, DSB repair, and ATR signaling during mammalian meiosis. Elife *11*. 10.7554/ELIFE.68677.

30. Manke, I.A., Lowery, D.M., Nguyen, A., and Yaffe, M.B. (2003). BRCT repeats as phosphopeptide-binding modules involved in protein targeting. Science *302*, 636–639.

31. Rodriguez, M., Yu, X., Chen, J., and Songyang, Z. (2003). Phosphopeptide binding specificities of BRCA1 COOH-terminal (BRCT) domains. J. Biol. Chem. *278*, 52914–52918.

32. Jeon, Y., Park, M.K., Kim, S.M., Bae, J.S., Lee, C.W., and Lee, H. (2019). TopBP1 deficiency impairs the localization of proteins involved in early recombination and results in meiotic chromosome defects during spermatogenesis. Biochem. Biophys. Res. Commun. *508*. 10.1016/j.bbrc.2018.12.001.

33. Perera, D., Perez-Hidalgo, L., Moens, P.B., Reini, K., Lakin, N., Syväoja, J.E., San-Segundo, P.A., and Freire, R. (2004). TopBP1 and ATR Colocalization at Meiotic Chromosomes: Role of TopBP1/Cut5 in the Meiotic Recombination Checkpoint. Mol. Biol. Cell *15*, 1568–1579.

34. ElInati, E., Russell, H.R., Ojarikre, O.A., Sangrithi, M., Hirota, T., De Rooij, D.G., McKinnon, P.J., and Turner, J.M.A. (2017). DNA damage response protein TOPBP1 regulates X chromosome silencing in the mammalian germ line. Proc. Natl. Acad. Sci. U. S. A. *114*, 12536–12541.

35. Parrilla-Castellar, E.R., Arlander, S.J.H., and Karnitz, L. (2004). Dial 9–1–1 for DNA damage: the Rad9–Hus1–Rad1 (9–1–1) clamp complex. DNA Repair *3*, 1009–1014.

36. Broering, T.J., Alavattam, K.G., Sadreyev, R.I., Ichijima, Y., Kato, Y., Hasegawa, K., Camerini-Otero, R.D., Lee, J.T., Andreassen, P.R., and Namekawa, S.H. (2014). BRCA1 establishes DNA damage signaling and pericentric heterochromatin of the X chromosome in male meiosis. J. Cell Biol. *205*, 663–675.

37. Reini, K., Uitto, L., Perera, D., Moens, P.B., Freire, R., and Syväoja, J.E. (2004). TopBPI localises to centrosomes in mitosis and to chromosome cores in meiosis. Chromosoma *112*. 10.1007/s00412-004-0277-5.

38. Moens, P.B., Tarsounas, M., Morita, T., Habu, T., Rottinghaus, S.T., Freire, R., Jackson, S.P., Barlow, C., and Wynshaw-Boris, A. (1999). The association of ATR protein with mouse meiotic chromosome cores. Chromosoma *108*. 10.1007/s004120050356.

39. Xu, Y., and Qiao, H. (2021). A Hypothesis: Linking Phase Separation to Meiotic Sex Chromosome Inactivation and Sex-Body Formation. Front Cell Dev Biol *9*, 674203.

40. Turner, J.M.A., Aprelikova, O., Xu, X., Wang, R., Kim, S., Chandramouli, G.V.R., Barrett, J.C., Burgoyne, P.S., and Deng, C.-X. (2004). BRCA1, histone H2AX phosphorylation, and male meiotic sex chromosome inactivation. Curr. Biol. *14*, 2135–2142.

41. Shin, Y.-H., Choi, Y., Erdin, S.U., Yatsenko, S.A., Kloc, M., Yang, F., Jeremy Wang, P., Meistrich, M.L., and Rajkovic, A. (2010). Hormad1 Mutation Disrupts Synaptonemal Complex Formation, Recombination, and Chromosome Segregation in Mammalian Meiosis. PLoS Genetics *6*, e1001190. 10.1371/journal.pgen.1001190.

42. Ichijima, Y., Ichijima, M., Lou, Z., Nussenzweig, A., Daniel Camerini-Otero, R., Chen, J., Andreassen, P.R., and Namekawa, S.H. (2011). MDC1 directs chromosome-wide silencing of the sex chromosomes in male germ cells. Genes and Development *25*, 959–971.

43. O'Driscoll, M., Dobyns, W.B., Van Hagen, J.M., and Jeggo, P.A. (2007). Cellular and clinical impact of haploinsufficiency for genes involved in ATR signaling. Am. J. Hum. Genet. *81*. 10.1086/518696.

44. Brown, E.J., and Baltimore, D. (2000). ATR disruption leads to chromosomal fragmentation and early embryonic lethality. Genes and Development *14*. 10.1101/gad.14.4.397.

45. De Klein, A., Muijtjens, M., Van Os, R., Verhoeven, Y., Smit, B., Carr, A.M., Lehmann, A.R., and Hoeijmakers, J.H.J. (2000). Targeted disruption of the cell-cycle checkpoint gene ATR leads to early embryonic lethality in mice. Curr. Biol. *10*. 10.1016/S0960-9822(00)00447-4.

46. O'Driscoll, M. (2009). Mouse models for ATR deficiency. DNA Repair *8*. 10.1016/j.dnarep.2009.09.001.

47. Yamane, K., Wu, X., and Chen, J. (2002). A DNA damage-regulated BRCT-containing protein, TopBP1, is required for cell survival. Mol. Cell. Biol. *22*, 555–566.

48. Jeon, Y., Ko, E., Lee, K.Y., Ko, M.J., Park, S.Y., Kang, J., Jeon, C.H., Lee, H., and Hwang, D.S. (2011). TopBP1 deficiency causes an early embryonic lethality and induces cellular senescence in primary cells. J. Biol. Chem. *286*, 5414–5422.

49. Zhou, Z.W., Liu, C., Li, T.L., Bruhn, C., Krueger, A., Min, W.K., Wang, Z.Q., and Carr, A.M. (2013). An Essential Function for the ATR-Activation-Domain (AAD) of TopBP1 in Mouse Development and Cellular Senescence. PLoS Genet. *9*. 10.1371/journal.pgen.1003702.

50. Inselman, A., Eaker, S., and Handel, M.A. (2003). Temporal expression of cell cycle-related proteins during spermatogenesis: establishing a timeline for onset of the meiotic divisions. Cytogenet. Genome Res. *103*, 277–284.

51. Falck, J., Coates, J., and Jackson, S.P. (2005). Conserved modes of recruitment of ATM, ATR and DNA-PKcs to sites of DNA damage. Nature *434*, 605–611.

52. Blackford, A.N., and Jackson, S.P. (2017). ATM, ATR, and DNA-PK: The Trinity at the Heart of the DNA Damage Response. Mol. Cell *66*, 801–817.

53. Maréchal, A., and Zou, L. (2013). DNA damage sensing by the ATM and ATR kinases. Cold Spring Harb. Perspect. Biol. *5*. 10.1101/cshperspect.a012716.

54. Hartwell, L.H., and Kastan, M.B. (1994). Cell cycle control and cancer. Science *266*, 1821–1828.

55. Shiloh, Y. (2003). ATM and related protein kinases: safeguarding genome integrity. Nat. Rev. Cancer *3*, 155–168.

56. Lanz, M.C., Dibitetto, D., and Smolka, M.B. (2019). DNA damage kinase signaling: checkpoint and repair at 30 years. EMBO J. *38*, e101801.

57. Kwon, M., Leibowitz, M.L., and Lee, J.-H. (2020). Small but mighty: the causes and consequences

of micronucleus rupture. Experimental & Molecular Medicine *52*, 1777–1786. 10.1038/s12276-020-00529-z.

58. Wang, J., Gong, Z., and Chen, J. (2011). MDC1 collaborates with TopBP1 in DNA replication checkpoint control. J. Cell Biol. *193*, 267–273.

59. Balbo Pogliano, C., Ceppi, I., Giovannini, S., Petroulaki, V., Palmer, N., Uliana, F., Gatti, M., Kasaciunaite, K., Freire, R., Seidel, R., et al. (2022). The CDK1-TOPBP1-PLK1 axis regulates the Bloom's syndrome helicase BLM to suppress crossover recombination in somatic cells. Sci Adv *8*, eabk0221.

60. Wang, J., Chen, J., and Gong, Z. (2013). TopBP1 controls BLM protein level to maintain genome stability. Mol. Cell *52*, 667–678.

61. Carpenter, A.T. (1979). Recombination nodules and synaptonemal complex in recombination-defective females of Drosophila melanogaster. Chromosoma *75*, 259–292.

62. Abe, H., Alavattam, K.G., Kato, Y., Castrillon, D.H., Pang, Q., Andreassen, P.R., and Namekawa, S.H. (2018). CHEK1 coordinates DNA damage signaling and meiotic progression in the male germline of mice. Hum. Mol. Genet. *27*, 1136–1149.

63. Thompson, A., Schäfer, J., Kuhn, K., Kienle, S., Schwarz, J., Schmidt, G., Neumann, T., Johnstone, R., Mohammed, A.K.A., and Hamon, C. (2003). Tandem mass tags: a novel quantification strategy for comparative analysis of complex protein mixtures by MS/MS. Anal. Chem. *75*, 1895–1904.

64. Sims, J.R., Faça, V.M., Pereira, C., Ascenção, C., Comstock, W., Badar, J., Arroyo-Martinez, G.A., Freire, R., Cohen, P.E., Weiss, R.S., et al. (2022). Phosphoproteomics of ATR signaling in mouse testes. Elife *11*. 10.7554/eLife.68648.

65. Cohen, S., Puget, N., Lin, Y.-L., Clouaire, T., Aguirrebengoa, M., Rocher, V., Pasero, P., Canitrot, Y., and Legube, G. (2018). Senataxin resolves RNA:DNA hybrids forming at DNA double-strand breaks to prevent translocations. Nat. Commun. *9*, 533.

66. Yeo, A.J., Becherel, O.J., Luff, J.E., Graham, M.E., Richard, D., and Lavin, M.F. (2015). Senataxin controls meiotic silencing through ATR activation and chromatin remodeling. Cell Discovery *1*. 10.1038/celldisc.2015.25.

67. Becherel, O.J., Yeo, A.J., Stellati, A., Heng, E.Y.H., Luff, J., Suraweera, A.M., Woods, R., Fleming, J., Carrie, D., McKinney, K., et al. (2013). Senataxin Plays an Essential Role with DNA Damage Response Proteins in Meiotic Recombination and Gene Silencing. PLoS Genet. *9*. 10.1371/journal.pgen.1003435.

68. Ichijima, Y., Sin, H.S., and Namekawa, S.H. (2012). Sex chromosome inactivation in germ cells: Emerging roles of DNA damage response pathways. Cellular and Molecular Life Sciences *69*. 10.1007/s00018-012-0941-5.

69. Lau, X., Munusamy, P., Ng, M.J., and Sangrithi, M. (2020). Single-Cell RNA Sequencing of the Cynomolgus Macaque Testis Reveals Conserved Transcriptional Profiles during Mammalian Spermatogenesis. Dev. Cell *54*, 548-566.e7.

70. Khalil, A.M., Boyar, F.Z., and Driscoll, D.J. (2004). Dynamic histone modifications mark sex

chromosome inactivation and reactivation during mammalian spermatogenesis. Proc. Natl. Acad. Sci. U. S. A. *101*, 16583–16587.

71. Alavattam, K.G., Maezawa, S., Andreassen, P.R., and Namekawa, S.H. (2022). Meiotic sex chromosome inactivation and the XY body: a phase separation hypothesis. Cellular and Molecular Life Sciences *79*. 10.1007/s00018-021-04075-3.

72. Jung, M., Wells, D., Rusch, J., Ahmad, S., Marchini, J., Myers, S.R., and Conrad, D.F. (2019). Unified single-cell analysis of testis gene regulation and pathology in five mouse strains. eLife *8*. 10.7554/elife.43966.

73. Grive, K.J., Hu, Y., Shu, E., Grimson, A., Elemento, O., Grenier, J.K., and Cohen, P.E. (2019). Dynamic transcriptome profiles within spermatogonial and spermatocyte populations during postnatal testis maturation revealed by single-cell sequencing. PLoS Genet. *15*, e1007810.

74. Hirota, T., Blakeley, P., Sangrithi, M.N., Mahadevaiah, S.K., Encheva, V., Snijders, A.P., ElInati, E., Ojarikre, O.A., de Rooij, D.G., Niakan, K.K., et al. (2018). SETDB1 Links the Meiotic DNA Damage Response to Sex Chromosome Silencing in Mice. Dev. Cell *47*, 645-659.e6.

75. Modzelewski, A.J., Holmes, R.J., Hilz, S., Grimson, A., and Cohen, P.E. (2012). AGO4 regulates entry into meiosis and influences silencing of sex chromosomes in the male mouse germline. Dev. Cell *23*, 251–264.

76. Chen, Y., Zheng, Y., Gao, Y., Lin, Z., Yang, S., Wang, T., Wang, Q., Xie, N., Hua, R., Liu, M., et al. (2018). Single-cell RNA-seq uncovers dynamic processes and critical regulators in mouse spermatogenesis. Cell Res. *28*, 879–896.

77. Greenlee, A.R., Shiao, M.-S., Snyder, E., Buaas, F.W., Gu, T., Stearns, T.M., Sharma, M., Murchison, E.P., Puente, G.C., and Braun, R.E. (2012). Deregulated sex chromosome gene expression with male germ cell-specific loss of Dicer1. PLoS One *7*, e46359.

78. Bennett, C.L., and La Spada, A.R. (2018). Senataxin, A Novel Helicase at the Interface of RNA Transcriptome Regulation and Neurobiology: From Normal Function to Pathological Roles in Motor Neuron Disease and Cerebellar Degeneration. In RNA Metabolism in Neurodegenerative Diseases, R. Sattler and C. J. Donnelly, eds. (Springer International Publishing), pp. 265–281.

79. Santos-Pereira, J.M., and Aguilera, A. (2015). R loops: new modulators of genome dynamics and function. Nat. Rev. Genet. *16*, 583–597.

80. Marnef, A., and Legube, G. (2020). m6A RNA modification as a new player in R-loop regulation. Nat. Genet. *52*, 27–28.

81. Rockmill, B., Fung, J.C., Branda, S.S., and Roeder, G.S. (2003). The Sgs1 helicase regulates chromosome synapsis and meiotic crossing over. Curr. Biol. *13*, 1954–1962.

82. Holloway, J.K., Morelli, M.A., Borst, P.L., and Cohen, P.E. (2010). Mammalian BLM helicase is critical for integrating multiple pathways of meiotic recombination. J. Cell Biol. *188*, 779–789.

83. Lenzi, M.L., Smith, J., Snowden, T., Kim, M., Fishel, R., Poulos, B.K., and Cohen, P.E. (2005). Extreme heterogeneity in the molecular events leading to the establishment of chiasmata during meiosis i in human oocytes. Am. J. Hum. Genet. *76*, 112–127.

84. Danielsen, J.M.R., Larsen, D.H., Freire, R., Falck, J., Bartek, J., Lukas, J., and Others (2009). HCLK2 is required for activity of the DNA damage response kinase ATR. J. Biol. Chem. *284*, 4140–4147.

85. Wojtasz, L., Cloutier, J.M., Baumann, M., Daniel, K., Varga, J., Fu, J., Anastassiadis, K., Stewart, A.F., Reményi, A., Turner, J.M.A., et al. (2012). Meiotic DNA double-strand breaks and chromosome asynapsis in mice are monitored by distinct HORMAD2-independent and -dependent mechanisms. Genes Dev. *26*, 958–973.

86. Holloway, J.K., Sun, X., Yokoo, R., Villeneuve, A.M., and Cohen, P.E. (2014). Mammalian CNTD1 is critical for meiotic crossover maturation and deselection of excess precrossover sites. J. Cell Biol. *205*, 633–641.

87. Kakarougkas, A., Ismail, A., Katsuki, Y., Freire, R., Shibata, A., and Jeggo, P.A. (2013). Co-operation of BRCA1 and POH1 relieves the barriers posed by 53BP1 and RAP80 to resection. Nucleic Acids Res. *41*, 10298–10311.

88. Modzelewski, A.J., Hilz, S., Crate, E.A., Schweidenback, C.T.H., Fogarty, E.A., Grenier, J.K., Freire, R., Cohen, P.E., and Grimson, A. (2015). Dgcr8 and Dicer are essential for sex chromosome integrity during meiosis in males. J. Cell Sci. *128*, 2314–2327.

89. Hao, Y., Hao, S., Andersen-Nissen, E., Mauck, W.M., 3rd, Zheng, S., Butler, A., Lee, M.J., Wilk, A.J., Darby, C., Zager, M., et al. (2021). Integrated analysis of multimodal single-cell data. Cell *184*, 3573-3587.e29.

90. Leek, J.T., Johnson, W.E., Parker, H.S., Fertig, E.J., and Jaffe, A.E. sva: Surrogate Variable Analysis R package version 3.10. 0. DOI10 B.

91. Aran, D., Looney, A.P., Liu, L., Wu, E., Fong, V., Hsu, A., Chak, S., Naikawadi, R.P., Wolters, P.J., Abate, A.R., et al. (2019). Reference-based analysis of lung single-cell sequencing reveals a transitional profibrotic macrophage. Nat. Immunol. *20*, 163–172.

92. Wickham, H. (2007). Reshaping Data with the reshape Package. J. Stat. Softw. *21*, 1–20.

93. Durinck, S., Spellman, P.T., Birney, E., and Huber, W. (2009). Mapping identifiers for the integration of genomic datasets with the R/Bioconductor package biomaRt. Nat. Protoc. *4*, 1184–1191.

94. Kassambara, A. (2019). GGPlot2 Essentials: Great Data Visualization in R (Independently Published).

95. Wickham, H., Averick, M., Bryan, J., Chang, W., McGowan, L., François, R., Grolemund, G., Hayes, A., Henry, L., Hester, J., et al. (2019). Welcome to the tidyverse. J. Open Source Softw. *4*, 1686.

96. Korsunsky, I., Millard, N., Fan, J., Slowikowski, K., Zhang, F., Wei, K., Baglaenko, Y., Brenner, M., Loh, P.-R., and Raychaudhuri, S. (2019). Fast, sensitive and accurate integration of single-cell data with Harmony. Nat. Methods *16*, 1289–1296.

97. Carlson, M., Falcon, S., Pages, H., and Li, N. org. Mm. eg. db: Genome wide annotation for Mouse. R package version.

98. Wei, T., and Simko, V. (2017). R package “corrplot”: Visualization of a Correlation Matrix (Version 0.84).

99. Balmus, G., Zhu, M., Mukherjee, S., Lyndaker, A.M., Hume, K.R., Lee, J., Riccio, M.L., Reeves, A.P., Sutter, N.B., Noden, D.M., et al. (2012). Disease severity in a mouse model of ataxia telangiectasia is modulated by the DNA damage checkpoint gene Hus1. Hum. Mol. Genet. *21*, 3408–3420.

100. Kolas, N.K., Svetlanov, A., Lenzi, M.L., Macaluso, F.P., Lipkin, S.M., Liskay, R.M., Greally, J., Edelmann, W., and Cohen, P.E. (2005). Localization of MMR proteins on meiotic chromosomes in mice indicates distinct functions during prophase I. J. Cell Biol. *171*, 447–458.

101. Eng, J.K., Jahan, T.A., and Hoopmann, M.R. (2013). Comet: An open-source MS/MS sequence database search tool. PROTEOMICS *13*, 22–24. 10.1002/pmic.201200439.

102. Bastos de Oliveira, F.M., Kim, D., Cussiol, J.R., Das, J., Jeong, M.C., Doerfler, L., Schmidt, K.H., Yu, H., and Smolka, M.B. (2015). Phosphoproteomics reveals distinct modes of Mec1/ATR signaling during DNA replication. Mol. Cell *57*, 1124–1132.

103. Rodríguez-Casuriaga, R., Santiñaque, F.F., Folle, G.A., Souza, E., López-Carro, B., and Geisinger, A. (2014). Rapid preparation of rodent testicular cell suspensions and spermatogenic stages purification by flow cytometry using a novel blue-laser-excitable vital dye. MethodsX *1*, 239–243.

Figure legends

Figure 1. A new TOPBP1 mutant separating its role in fertility from organismal viability.

A) Schematic showing mutations in the *Topbp1 B5* allele. B) Body mass (*Topbp1*$^{+/+}$ Mean = 25.26, SD = 2.38; *Topbp1*$^{B5/B5}$ Mean = 26.43, SD = 2.28, n = 9) and C) appearance of *Topbp1*$^{B5/B5}$ and *Topbp1*$^{+/+}$ littermate mice. D) Effect of full body IR (7 Gy) on changes in body mass of *Topbp1*$^{B5/B5}$ and *Topbp1*$^{+/+}$ littermate mice E) Breeding scheme and resulting litters. F) and G) Comparison of testes size (*Topbp1*$^{+/+}$ Mean = 0.038, SD = 0.006; *Topbp1*$^{B5/B5}$ Mean = 0.011, SD = 0.004, n = 9), and H) sperm count, of *Topbp1*$^{B5/B5}$ and *Topbp1*$^{+/+}$ littermate mice (*Topbp1*$^{+/+}$ Mean = 2.1 x 10^7, SD = 6x 10^6; *Topbp1*$^{B5/B5}$ Mean = 0.0, SD = 0.0, n = 9). I) H&E-stained histological testes sections displaying loss of cellularity in *Topbp1*$^{B5/B5}$. Green arrow = spermatogonia, Red arrow = healthy spermatocyte, Blue arrow = dying spermatocyte. J) and K) TUNEL assay performed on histological testes sections (*Topbp1*$^{+/+}$ Mean = 0.36, SD = 0.15; *Topbp1*$^{B5/B5}$ Mean = 4.80, SD = 0.43, n = 3). L) Meiotic spreads stained for SYCP3, SYCP1 and H1t. **** = p< 0.0001, n = number of mice. p-Values were calculated using Welch's unpaired *t*-test in GraphPad.

Figure 2. *Topbp1*$^{B5/B5}$ MEFs display no detectable DDR defects.

A) MEFs obtained from littermate mice of indicated genotypes were subjected to clonogenic survival assay in the indicated concentrations of hydroxyurea, or C) phleomycin. B) and D) Quantification of clonogenic survival assays from A and C, respectively, performed in biological and experimental triplicates. D) Western blot for indicated DDR markers in MEFs obtained from *Topbp1*$^{B5/B5}$ and *Topbp1*$^{+/+}$ littermate mice. The data from MEFs were performed using littermate pairs and validated using a second pair of *Topbp1*$^{B5/B5}$ and *Topbp1*$^{+/+}$ littermate mice. E) Immunofluorescence of MDC1 and phosphoH2AX_S139-stained nuclei from *Topbp1*$^{B5/B5}$ and *Topbp1*$^{+/+}$ MEFs treated with IR (7 Gy).

Figure 3. Markers of DNA repair, synapsis, sex body formation and TOPBP1 localization are mostly normal in *Topbp1*$^{B5/B5}$ spermatocytes.

A) Meiotic spreads showing *Topbp1*$^{+/+}$ and *Topbp1*$^{B5/B5}$ spermatocytes stained with SYCP3 and γH2AX, prepared as described in methods. B) Quantification of γH2AX-stained pachytene spreads, upper graph autosomal chromosomes (each dot represents the average of signal from all autosomes in each mouse) and bottom, XY body. C) Meiotic spreads showing *Topbp1*$^{+/+}$ and *Topbp1*$^{B5/B5}$ pachytene spermatocytes stained with SYCP3 and RAD51. D) Quantification of RAD51 foci/cell of mid-pachytene meiotic spreads. E) Meiotic spreads showing *Topbp1*$^{+/+}$ and *Topbp1*$^{B5/B5}$ pachytene spermatocytes stained with SYCP3 and SYCP1. F) Meiotic spreads showing *Topbp1*$^{+/+}$ and *Topbp1*$^{B5/B5}$ pachytene spermatocytes

stained with SYCP3 and TOPBP1. Quantification of TOPBP1-stained pachytene spreads G) X and Y chromosome cores, and H) X and Y chromatin loops. n = number of mice. p-Values were calculated using Welch's unpaired *t*-test in GraphPad.

Figure 4. *Topbp1*$^{B5/B5}$ spermatocytes display normal localization of ATR, BRCA1, MDC1 and pMDC1-T4.

A-H) Meiotic spreads stained for indicated proteins and related quantification in *Topbp1*$^{+/+}$ and *Topbp1*$^{B5/B5}$ pachytene spermatocytes. I) Table summarizing the normal or disrupted ATR and TOPBP1-dependent events during male fertility accessed in *Topbp1*$^{B5/B5}$. n = number of mice. p-Values were calculated using Welch's unpaired *t*-test in GraphPad.

Figure 5. Defective SETX phosphorylation and localization in *Topbp1*$^{B5/B5}$ spermatocytes.

A) Scatter plot of phosphoproteomic datasets corresponding to *Topbp1*$^{+/+}$/*Topbp1*$^{B5/B}$ (Y axis) and *Topbp1*$^{+/+}$(vehicle)/*Topbp1*$^{+/+}$(AZ20) (X axis) from whole testes of mice. B) SETX phosphopeptides identified in the *Topbp1*$^{+/+}$/*Topbp1*$^{B5/B}$ phosphoproteomic experiment shown in A. Red: reduced in *Topbp1*$^{B5/B}$ mutant; Blue: unchanged. C) Meiotic spreads showing pachytene spermatocytes from *Topbp1*$^{+/+}$ and *Topbp1*$^{B5/B5}$ mice stained with SYCP3 and SETX in regular immunofluorescence, and D) 3D-SIM analysis of meiotic spread described in C. E) and F) Quantification of the intensity of SETX chromatin loops and cores of the XY chromosomes, respectively. * $p < 0.05$, n = number of mice. p-Values were calculated using Welch's unpaired *t*-test in GraphPad.

Figure 6. Single cell RNAseq reveals that *Topbp1*$^{B5/B5}$ spermatocytes initiate MSCI but fail to promote full silencing.

A) scRNAseq workflow for isolation and purification of single cells for RNA-seq. B) UMAP analysis of sub-clusters captured in the scRNAseq. C) UMAP analysis of sub-clusters captured in the scRNAseq of *Topbp1*$^{+/+}$. D) UMAP analysis of sub-clusters captured in the scRNAseq of *Topbp1*$^{+/+}$ (gray) and *Topbp1*$^{B5/B5}$ (blue). E) Violin plots displaying the ratio of the average expression of X chromosome genes by the average expression of chromosome 9 genes at different stages of spermatogenesis for *Topbp1*$^{+/+}$ and *Topbp1*$^{B5/B5}$ cells.

Figure 7. Topbp1 regulates silencing dynamics of X genes at the Spermatocyte 3 stage.

A) Illustration of the gene markers used to define spermatocyte 1 as leptotene, spermatocyte 2 as zygotene, and spermatocyte 3 as pachytene; hypothetical examples illustrating the categorization of transitions in silencing dynamics between the stages of pre-leptotene (PL), spermatocyte 1 (SP1), spermatocyte 2 (SP2),

spermatocyte 3 (SP3). B) Number of genes in each of the categories described in A, during the different stage transitions. C) Examples of genes with altered silencing dynamics in the *Topbp1*$^{B5/B5}$, red = reduced silencing, blue = unaltered silencing and green = increased silencing D) Scatter plot showing the difference in RNA level between *Topbp1*$^{+/+}$ and *Topbp1*$^{B5/B5}$ for each of the indicated stage transitions. E) Scatter plot showing expression level of X-chromosome genes, normalized to pre-leptotene levels, in *Topbp1*$^{+/+}$ (gray) and *Topbp1*$^{B5/B5}$ (blue) at SP3. F) Graph plotting expression levels of X-chromosome genes, normalized to pre-leptotene levels, in *Topbp1*$^{+/+}$ (Y axis) and *Topbp1*$^{B5/B5}$ (X axis) and split in three categories based on the severity of silencing defect. G) Box plot showing PL expression levels of X-chromosome genes in each of the categories of silencing defect severity shown in F.

Figure 8. A new TOPBP1 mutant separates XY silencing from sex body formation.

Schematic of sub-stages of meiotic prophase I. In Wild-type mice, MSCI initiates following the accumulation of the DDR proteins at the XY chromosomes. During mid-pachytene, the XY body is fully formed, and transcription is restricted to the autosomes. In *Atr* or *Topbp1* CKOs, the sex body is not formed, and the DDR proteins are not sequestered to the XY. Asynapsis events and transcription of toxic genes at the sex chromosomes are observed, triggering mid-pachytene arrest. In *Topbp1*$^{B5/B5}$, MSCI initiates, the sex body is normally formed with normal recruitment of DDR proteins to the X and Y chromosomes, yet cells fail in the reinforcement/maintenance of silencing. Cells progress through mid-pachytene but not into diplotene.

Supplemental material

Supplemental Figure legends

Supplemental Figure 1. Genotyping of *Topbp1*$^{B5/B5}$ mice.

Sanger sequencing confirms the eight charge reversal point mutations on the BRCT 5 domain of TOPBP1 from homozygous *Topbp1*$^{B5/B5}$ mice.

Supplemental Figure 2. Survival assays of *Topbp1*$^{B5/B5}$ MEFs.

A) MEFs obtained from littermate mice (second independent litter) of indicated genotypes were subjected to clonogenic survival assay in the indicated concentrations of hydroxyurea, or B) phleomycin.

Supplemental Figure 3. Absence of an increased number of micronuclei in *Topbp1*$^{B5/B5}$ MEFs.

Immunofluorescence showing DAPI-stained nuclei and micronuclei quantification of *Topbp1*$^{+/+}$ and *Topbp1*$^{B5/B5}$ A) MEFs #1 and B) MEFs #2. (MEFs #2 is a second independent litter).

Supplemental Figure 4. TOPBP1-B5 shows disruption in binding 53BP1 and BLM.

A) HEK-293T cells were transfected with plasmids expressing wild-type TOPBP1 or indicated BRCT mutants (K155A - BRCT 1, K250A - BRCT 2, K704A - BRCT 5, K1713A - BRCT 7, and B5 - 8 mutations in BRCT 5), with a 3xFlag tag. After cell lysis and anti-Flag IP, lysate and elution were analyzed by western blot for the indicated proteins. B) IP-mass spectrometry of flagTOPBP1 wild type versus flag-TOPBP1-B5 was performed in silac-labeled HEK-293T cells. Cell transfections, lysis, protein IP, and elution were performed as described in A. From left to right, the TOPBP1 interactors were plotted from highest to lowest binding. The size of circles represents the number of peptide hits.

Supplemental Figure 5. *Topbp1*$^{B5/B5}$ MEFs show lower TOPBP1 protein abundance than *Topbp1* $^{+/+}$ MEFs.

Western blot probing TOPBP1 in MEFs, *Topbp1* $^{+/+}$, *Topbp1*$^{B5/+}$, and *Topbp1*$^{B5/B5}$ in two biological replicates.

Supplemental Figure 6. *Topbp1*$^{B5/B5}$ mid-pachytene spermatocytes show normal HORMAD1, HORMAD2, pHORMAD1 and pCHK1_S345 localization and intensities.

A) *Topbp1*$^{+/+}$ and *Topbp1*$^{B5/B5}$ pachytene spermatocytes stained with HORMAD1 and SYCP3, B) HORMAD2 and SYCP3, and C) pMDC1_T4 and SYCP3. D) Quantification of *Topbp1*$^{+/+}$ and *Topbp1*$^{B5/B5}$

mid-pachytene meiotic spreads stained with pMDC1_T4. E) *Topbp1*$^{+/+}$ and *Topbp1*$^{B5/B5}$ mid-pachytene spermatocytes stained with pCHK1_S345 and SYCP3. F) Quantification of *Topbp1*$^{+/+}$ and *Topbp1*$^{B5/B5}$ mid-pachytene meiotic spreads stained with pCHK1_S345. G) *Topbp1*$^{+/+}$ and *Topbp1*$^{B5/B5}$ mid-pachytene spermatocytes stained with pHORMAD1_S271 and SYCP3. H) Quantification of *Topbp1*$^{+/+}$ and *Topbp1*$^{B5/B5}$ mid-pachytene meiotic spreads stained with pHORMAD1_S271. n = number of mice.

Supplemental Figure 7. *Topbp1*$^{B5/B5}$ mid-pachytene spermatocytes show an increased number of MLH1 foci/cell but no difference in the number of MHL3 foci/cell.

A) Representative images and quantification of *Topbp1*$^{+/+}$ and *Topbp1*$^{B5/B5}$ mid-pachytene spermatocytes stained with MLH1 and SYCP3, and B) MLH3. n = number of mice. *** $p < 0.001$. p-Values were calculated using Welch's unpaired t-test in GraphPad.

Supplemental Figure 8. *Topbp1*$^{B5/B5}$ mid-pachytene spermatocytes form a normal sex body.

Topbp1$^{+/+}$ and *Topbp1*$^{B5/B5}$ mid-pachytene spermatocytes stained with DAPI and SYCP3.

Supplemental Figure 9. *Topbp1*$^{B5/B5}$ mid-pachytene spermatocytes show subtle defects/delays in the spreading of γH2AX at the XY chromosomes.

A) Quantification and representative images of *Topbp1*$^{B5/B5}$ mid-pachytene spermatocytes showing normal spreading of γH2AX in the XY chromosomes B) showing a defect/delay in the spreading of γH2AX at the PAR, C) showing a defect/delay in the spreading of γH2AX at the pericentromeric region of the Y chromosome, D) showing a spreading of γH2AX into an autosomal chromosome fused to the X chromosome, and E) showing other types of defects/delays in the spreading of γH2AX into the XY chromosomes. F) Percentage of the previously described defects found in *Topbp1*$^{+/+}$ or G) *Topbp1*$^{B5/B5}$ mid-pachytene spermatocytes. *$p < 0.05$, **$p < 0.01$, ***$p < 0.001$, and **** $p < 0.0001$. p-Values were calculated using Welch's unpaired t-test in GraphPad. n = number of mice.

Supplemental Figure 10. TOPBP1 is normally localized in all stages of prophase I in *Topbp1*$^{B5/B5}$.

Meiotic spreads showing *Topbp1*$^{+/+}$ and *Topbp1*$^{B5/B5}$ spermatocytes stained with SYCP3 and TOPBP1.

Supplemental Figure 11. 53BP1 localization in *Topbp1*$^{B5/B5}$ mid-pachytene spermatocytes.

Meiotic spreads and quantification of pachytene spermatocytes from *Topbp1*$^{+/+}$ and *Topbp1*$^{B5/B5}$ mice stained with SYCP3 and 53BP1. n = number of mice.

Supplemental Figure 12. *Topbp1*$^{B5/B5}$ pachytene spermatocytes do not exhibit any difference in CHD4, Sumo2-3, and USP7 intensities and localization compared to *Topbp1*$^{+/+}$.

A) Representative images and quantification of *Topbp1*$^{+/+}$ and *Topbp1*$^{B5/B5}$ mid-pachytene spermatocytes stained with CHD4 and SYCP3, B) Sumo2.3 and SYCP3, and C) USP7 and SYCP3. n = number of mice.

Supplemental Figure 13. *Topbp1*$^{B5/B5}$ pachytene spermatocytes show no difference in H3K9ac or K3K9me3 staining compared to *Topbp1*$^{+/+}$.

A) Representative images and quantification of *Topbp1*$^{+/+}$ and *Topbp1*$^{B5/B5}$ mid-pachytene spermatocytes stained with H3K9ac and SYCP3. B) Representative images and quantification of *Topbp1*$^{+/+}$ and *Topbp1*$^{B5/B5}$ early, mid, or late-pachytene spermatocytes stained with H3K9me3 and SYCP3 *Topbp1*$^{B5/B5}$ n = number of mice.

Supplemental Figure 14. *Topbp1*$^{B5/B5}$ pachytene spermatocytes display no difference in H3K27ac, H3K36me3 or K3K4me3 staining compared to *Topbp1*$^{+/+}$.

A) Representative images and quantification of *Topbp1*$^{+/+}$ and *Topbp1*$^{B5/B5}$ mid-pachytene spermatocytes stained with H3K27ac and SYCP3, and B) H3K36me3 and SYCP3. C) Representative images and quantification of *Topbp1*$^{+/+}$ and *Topbp1*$^{B5/B5}$ early and mid-pachytene spermatocytes stained with H3K4me3 and SYCP3. n = number of mice.

Supplemental Figure 15. *Topbp1*$^{B5/B5}$ pachytene spermatocytes display no difference in H4K16ac, H4ac or H2AK166ub staining compared to *Topbp1*$^{+/+}$.

A) Representative images and quantification of *Topbp1*$^{+/+}$ and *Topbp1*$^{B5/B5}$ mid-pachytene spermatocytes stained with H4K16ac and SYCP3, B) H4 and SYCP3, and C) H2AK166ub and SYCP3. n = number of mice.

Supplemental Figure 16. From early pachytene to beginning of late pachytene, *Topbp1*$^{B5/B5}$ spermatocytes exhibit the same intensity and localization pattern of H3K4me1 compared to *Topbp1*$^{+/+}$.

Representative images of *Topbp1*$^{+/+}$ and *Topbp1*$^{B5/B5}$ early, mid and late pachytene spermatocytes stained with H3K4me1 and SYCP3.

Supplemental figure 17. *Topbp1*$^{B5/B5}$ pachytene spermatocytes exhibit no differences in the intensity or localization patterns of RNApol2, pRNApol2_Ser2 or pRNApol2_ser5 compared to *Topbp1*$^{+/+}$.

A) Representative images and quantification of *Topbp1*$^{+/+}$ and *Topbp1*$^{B5/B5}$ mid-pachytene spermatocytes stained with RNApol2 and SYCP3, B) pRNApol2_Ser2 and SYCP3, and C) pRNApol2_Ser5 and SYCP3. n = number of mice.

Supplemental Figure 18. Genes used as markers to define the stages of the germ cells in the scRNAseq analysis.

UMAP plots showing markers for Spermatogonia (*Sal1* and *Dmrt1*), Spermatocytes (*Dazl*, *Id4*, *Sycp3*, and *Shcbp1l*), and Spermatids (*Acrv1*, *Oaz3* and *Prm2*).

Supplemental Figure 19. Genes used as markers to track spermatogenesis progression and form the 47 sub-cluster for all cells captured in the 10X platform in the scRNAseq analysis.

Bubble plot displaying gene markers and their respective pattern of expression during spermatogenesis.

Supplemental Figure 20. Genes used as markers of somatic cells captured in the scRNAseq analysis.

UMAP plots show markers for the somatic cells captured on the germ cell-enriched population, Endothelial and Hematopoietic (*Col1a2*, *Vcam1*, *Laptm5* and *Insl3*), Smooth muscle (*Acta2*) and Sertoli (*Ptgds* and *Wt1*).

Supplemental Figure 21. Analysis of sub-clusters of all cells captured in the 10X platform.

UMAP plot displaying the 47 sub-clusters of cells captured in the scRNAseq analysis.

Supplemental Figure 22. Analysis of the main 24 sub-clusters captured in the germ cells-enriched scRNAseq analysis.

UMAP plot showing 24 sub-clusters for spermatogonia, spermatocytes, round spermatids, spermatids, Sertoli, smooth muscle and endothelial and hematopoietic cells captured in the 10X platform.

Supplemental Figure 23. Spermatocytes from *Topbp1*$^{+/+}$ and *Topbp1*$^{B5/B5}$ show correlation greater than 0.9.

Plot of Pearson correlation values between cell groups separated by cluster and genotype using log-normalized average expression of all genes.

Supplemental Figure 24. *Topbp1*$^{B5/B5}$ pachytene spermatocytes show increased expression of X-linked genes.

Heatmap displaying the expression levels of X-chromosome genes in spermatocyte 3 stage (pachytene) of *Topbp1*$^{B5/B5}$ on the right and *Topbp1*$^{+/+}$ on the left. Each line represents a gene, and each row is a cell.

Supplemental Figure 25. *Topbp1*$^{B5/B5}$ pachytene spermatocytes show increased expression of XY "killer genes" and other X and Y genes typically used to illustrate MSCI defects.

Violin plots showing the level of expression and number of cells expressing the XY chromosome genes in SP3 (pachytene): *Zfy1*, *Zfy2*, *Kdm6a*, *Lamp2*, *Scml2*, *Zfx*, *Uba1y* and *Rhox13* in *Topbp1*$^{B5/B5}$ and in *Topbp1*$^{+/+}$. The Wilcoxon test was used to calculate the p-values. **p < 0.01, ***p < 0.001, and **** p < 0.0001.

Supplemental Figure 26. *Topbp1*$^{B5/B5}$ pachytene spermatocytes show increased expression of XY-linked genes.

Bar plots showing the number of cells expressing the XY chromosome genes in SP3 (pachytene): *Zfy1*, *Zfy2*, *Kdm6a*, *Lamp2*, *Scml2*, *Zfx*, *Uba1y* and *Rhox13* in *Topbp1*$^{B5/B5}$ and in *Topbp1*$^{+/+}$. Fisher's exact test was used to calculate the p-values. **p < 0.01, ***p < 0.001, and **** p < 0.0001.

Supplemental Figure 27. Analysis of the gene marker used to define the zygotene stage.

UMAP analysis of the gene *Gm960* was used as a gene marker to define the zygotene stage.

Supplemental Figure 28. Expression levels of genes with no defects, mild defects, and strong defects in *Topbp1*$^{B5/B5}$ and *Topbp1*$^{+/+}$.

Boxplot showing the expression levels of the clusters of genes with no defects, mild defects, and strong defects from pre-leptotene to Spermatocyte 3 (pachytene) in *Topbp1*$^{B5/B5}$ and *Topbp1*$^{+/+}$. The Wilcoxon rank-sum test was used to calculate the p-values. *p < 0.05, **p < 0.01, ***p < 0.001, and **** p < 0.0001.

Supplemental Figure 29. Quality control of the scRNAseq data.

Violin plots show the quality control for the scRNAseq data, displaying the distribution of gene counts, UMI counts, and mitochondrial gene percentage per library before filtering data.

Figure 1

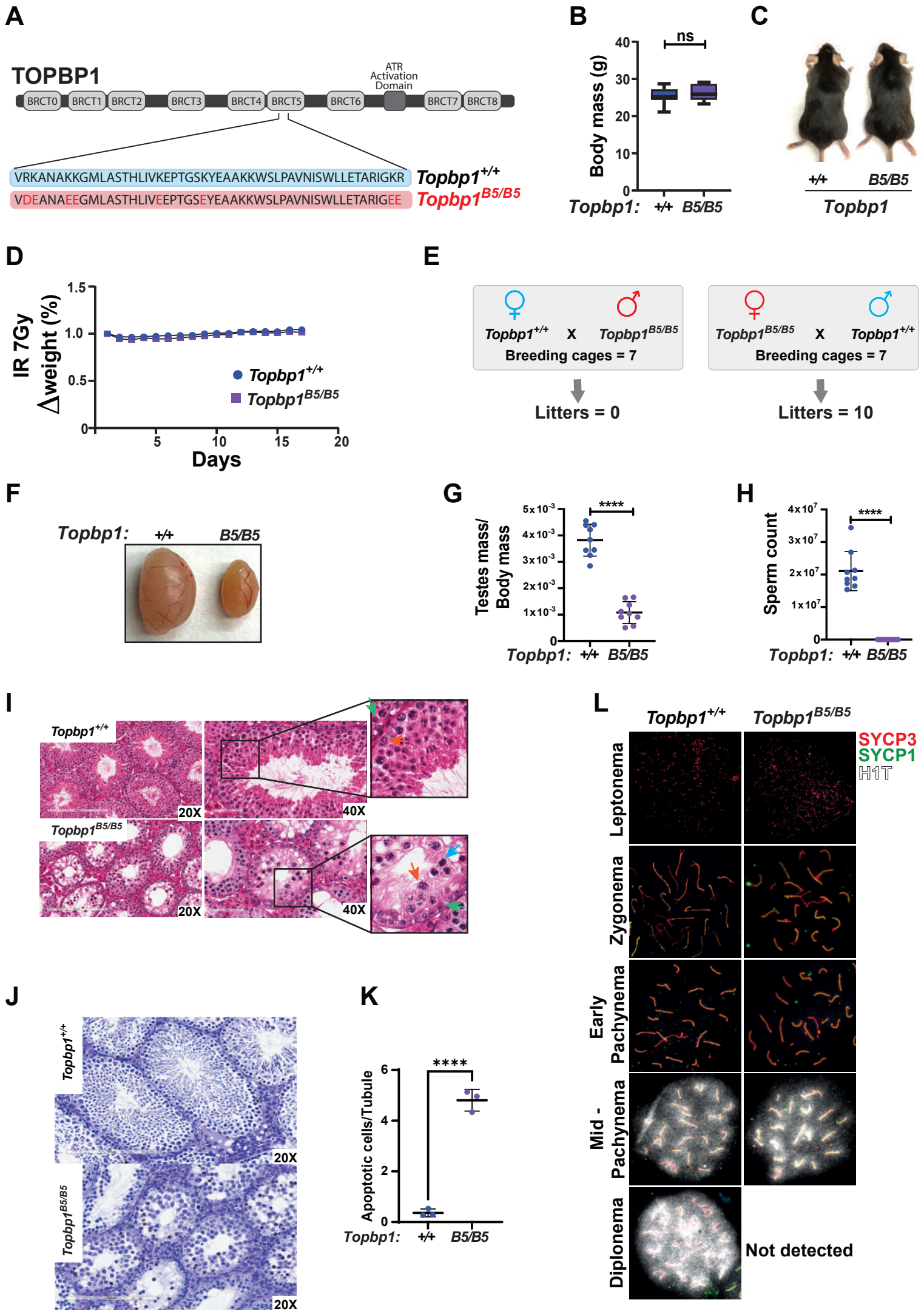
A
TOPBP1
ATR Activation Domain
BRCT0
BRCT1
BRCT2
BRCT3
BRCT4
BRCT5
BRCT6
BRCT7
BRCT8
VRKANAKKGMLASTHLIVKEPTGSKYEAAKKWSLPAVNISWLLETARIGKR
VDEANAEEGMLASTHLIVEEPTGSEYEAAKKWSLPAVNISWLLETARIGEE
Topbp1+/+
Topbp1B5/B5
B
ns
Body mass (g)
Topbp1: +/+ B5/B5
C
+/+
B5/B5
Topbp1
D
IR 7Gy
Δweight (%)
Topbp1+/+
Topbp1B5/B5
Days
E
Topbp1+/+ X Topbp1B5/B5
Breeding cages = 7
Litters = 0
Topbp1B5/B5 X Topbp1+/+
Breeding cages = 7
Litters = 10
F
Topbp1: +/+ B5/B5
G
Testes mass/ Body mass
****
Topbp1: +/+ B5/B5
H
Sperm count
****
Topbp1: +/+ B5/B5
I
Topbp1+/+
Topbp1B5/B5
20X
40X
J
Topbp1+/+
Topbp1B5/B5
20X
K
Apoptotic cells/Tubule
****
Topbp1: +/+ B5/B5
L
Topbp1+/+
Topbp1B5/B5
SYCP3
SYCP1
H1T
Leptonema
Zygonema
Early Pachynema
Mid - Pachynema
Diplonema
Not detected

Figure 2

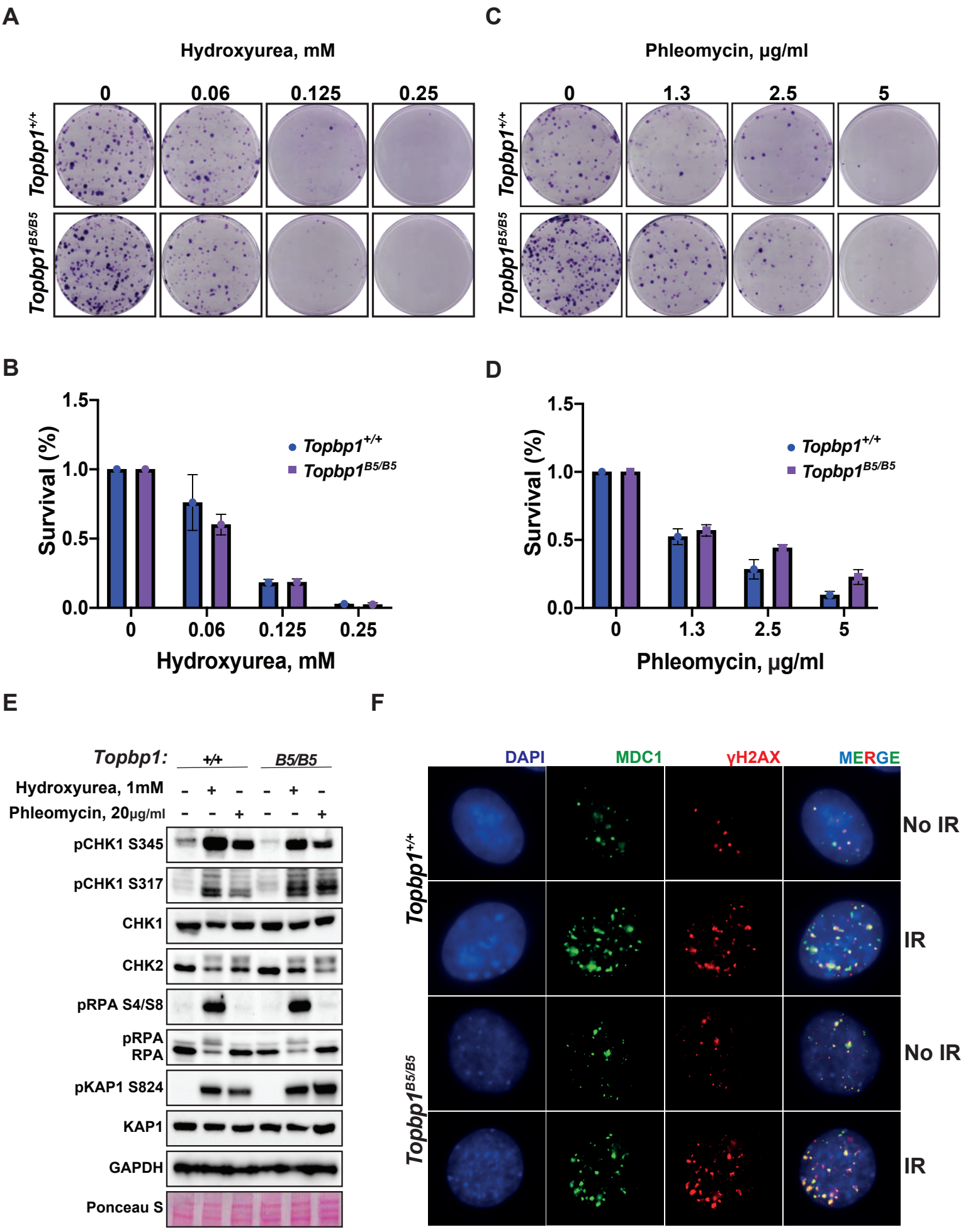
A
Hydroxyurea, mM
0
0.06
0.125
0.25
Topbp1+/+
Topbp1B5/B5
C
Phleomycin, µg/ml
0
1.3
2.5
5
Topbp1+/+
Topbp1B5/B5
B
Survival (%)
1.5
1.0
0.5
0.0
Topbp1+/+
Topbp1B5/B5
0
0.06
0.125
0.25
Hydroxyurea, mM
D
Survival (%)
1.5
1.0
0.5
0.0
Topbp1+/+
Topbp1B5/B5
0
1.3
2.5
5
Phleomycin, µg/ml
E
Topbp1:
+/+
B5/B5
Hydroxyurea, 1mM
Phleomycin, 20µg/ml
pCHK1 S345
pCHK1 S317
CHK1
CHK2
pRPA S4/S8
pRPA
RPA
pKAP1 S824
KAP1
GAPDH
Ponceau S
F
DAPI
MDC1
γH2AX
MERGE
Topbp1+/+
Topbp1B5/B5
No IR
IR
No IR
IR

Figure 3

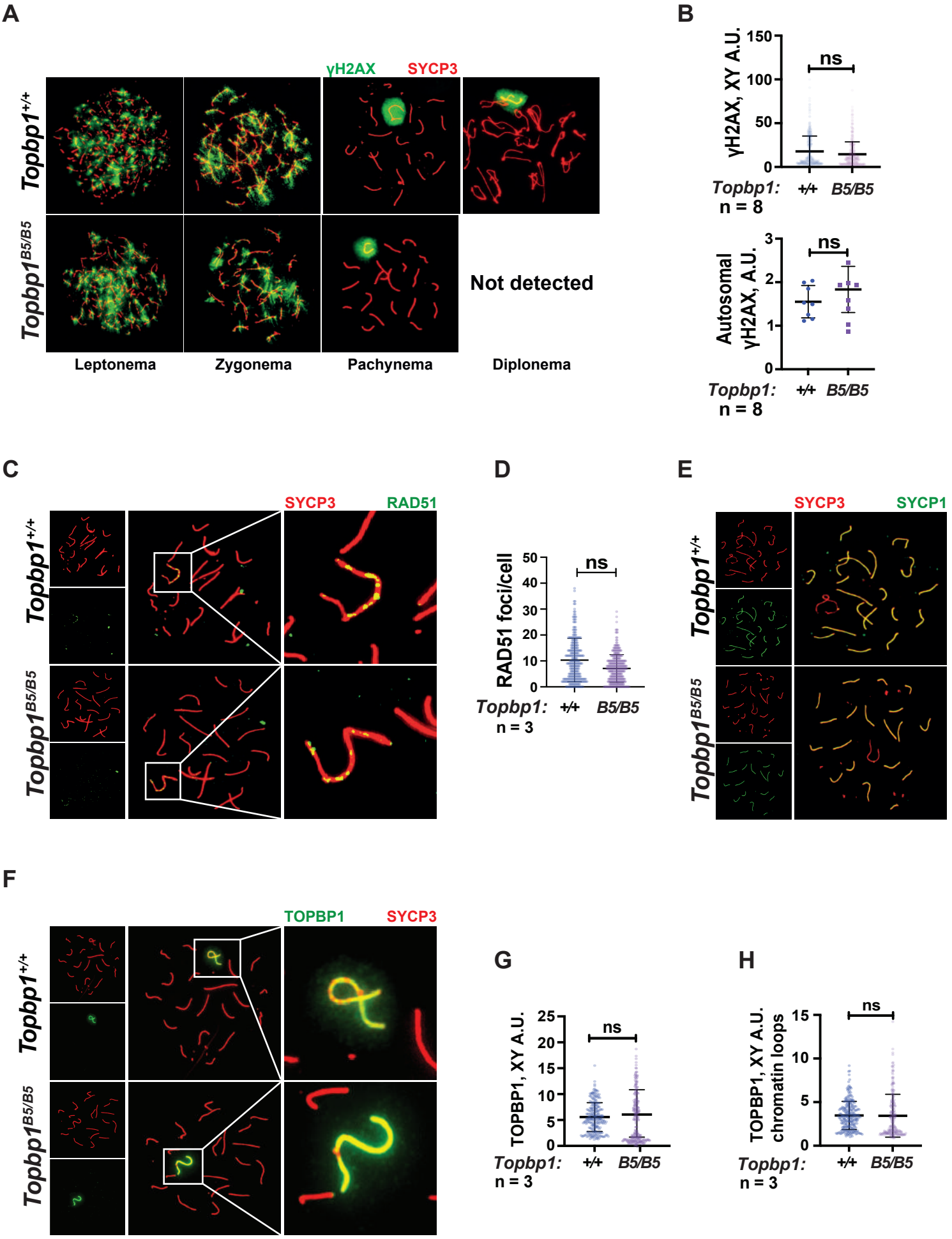
A
γH2AX
SYCP3
Topbp1+/+
Topbp1B5/B5
Not detected
Leptonema
Zygonema
Pachynema
Diplonema
B
γH2AX, XY A.U.
150
100
50
0
ns
Topbp1: +/+ B5/B5
n = 8
Autosomal γH2AX, A.U.
3
2
1
0
ns
Topbp1: +/+ B5/B5
n = 8
C
SYCP3
RAD51
Topbp1+/+
Topbp1B5/B5
D
RAD51 foci/cell
50
40
30
20
10
0
ns
Topbp1: +/+ B5/B5
n = 3
E
SYCP3
SYCP1
Topbp1+/+
Topbp1B5/B5
F
TOPBP1
SYCP3
Topbp1+/+
Topbp1B5/B5
G
TOPBP1, XY A.U.
25
20
15
10
5
0
ns
Topbp1: +/+ B5/B5
n = 3
H
TOPBP1, XY A.U. chromatin loops
15
10
5
0
ns
Topbp1: +/+ B5/B5
n = 3

Figure 4

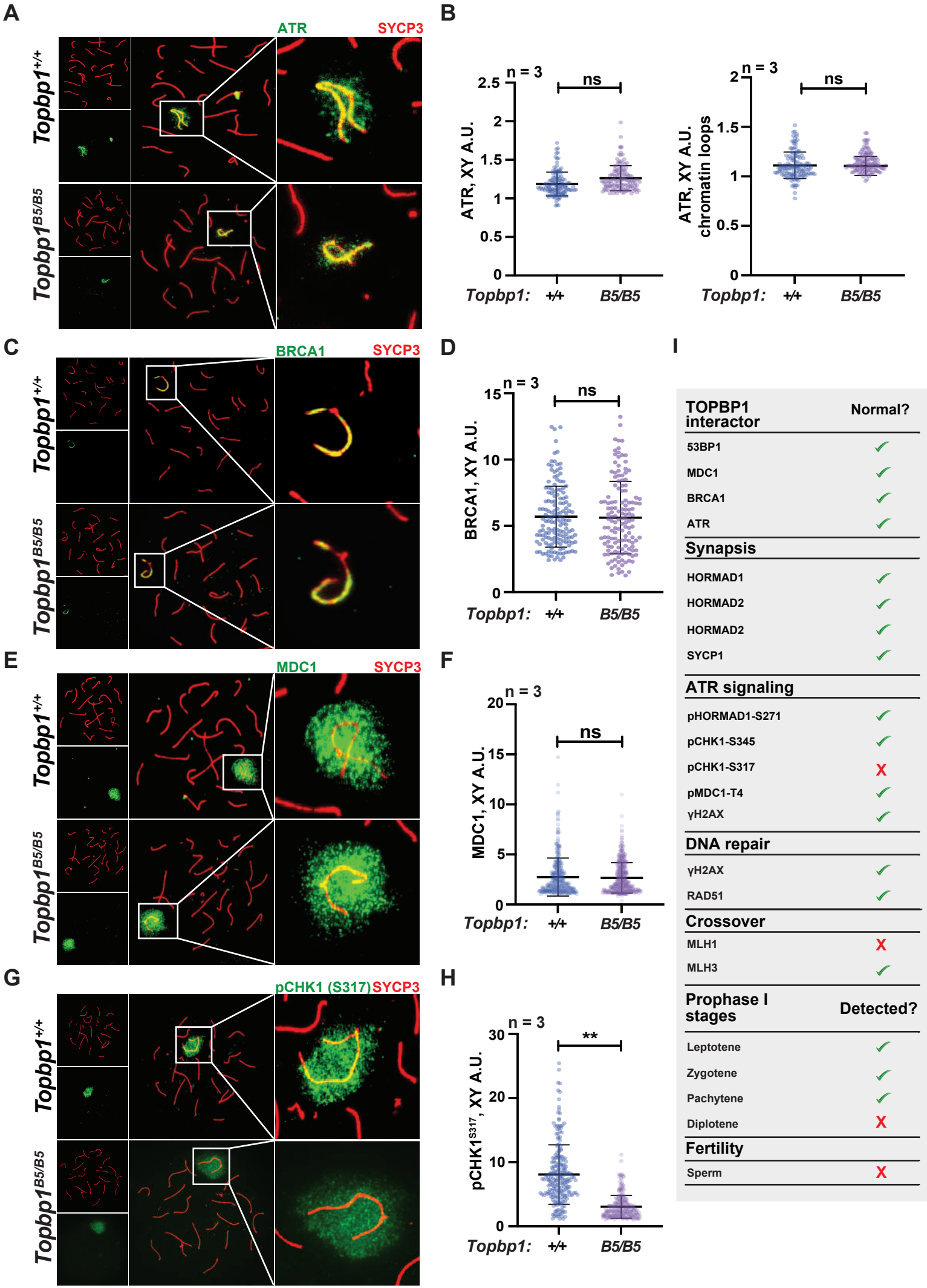

TOPBP1 interactor	Normal?
53BP1	✓
MDC1	✓
BRCA1	✓
ATR	✓
Synapsis	
HORMAD1	✓
HORMAD2	✓
HORMAD2	✓
SYCP1	✓
ATR signaling	
pHORMAD1-S271	✓
pCHK1-S345	✓
pCHK1-S317	X
pMDC1-T4	✓
γH2AX	✓
DNA repair	
γH2AX	✓
RAD51	✓
Crossover	
MLH1	X
MLH3	✓
Prophase I stages	**Detected?**
Leptotene	✓
Zygotene	✓
Pachytene	✓
Diplotene	X
Fertility	
Sperm	X

Figure 5

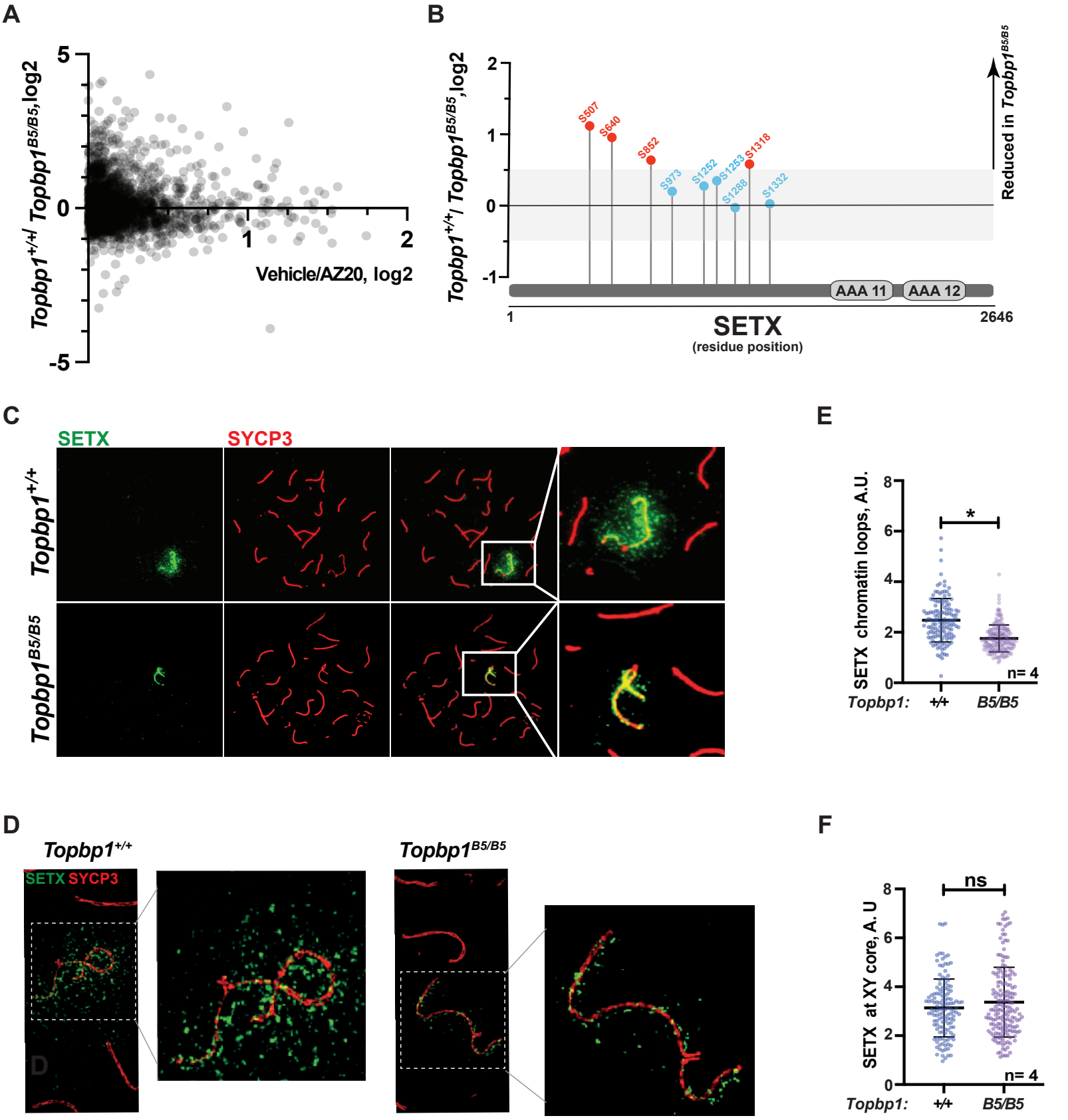
A
Topbp1+/+/ Topbp1B5/B5,log2
Vehicle/AZ20, log2
B
Topbp1+/+/ Topbp1B5/B5,log2
Reduced in Topbp1B5/B5
S507
S640
S852
S973
S1252
S1253
S1318
S1288
S1332
AAA 11
AAA 12
SETX
(residue position)
C
SETX
SYCP3
Topbp1+/+
Topbp1B5/B5
E
SETX chromatin loops, A.U.
n= 4
Topbp1:
+/+
B5/B5
D
Topbp1+/+
Topbp1B5/B5
SETX SYCP3
F
SETX at XY core, A. U
ns
n= 4
Topbp1:
+/+
B5/B5

Figure 6

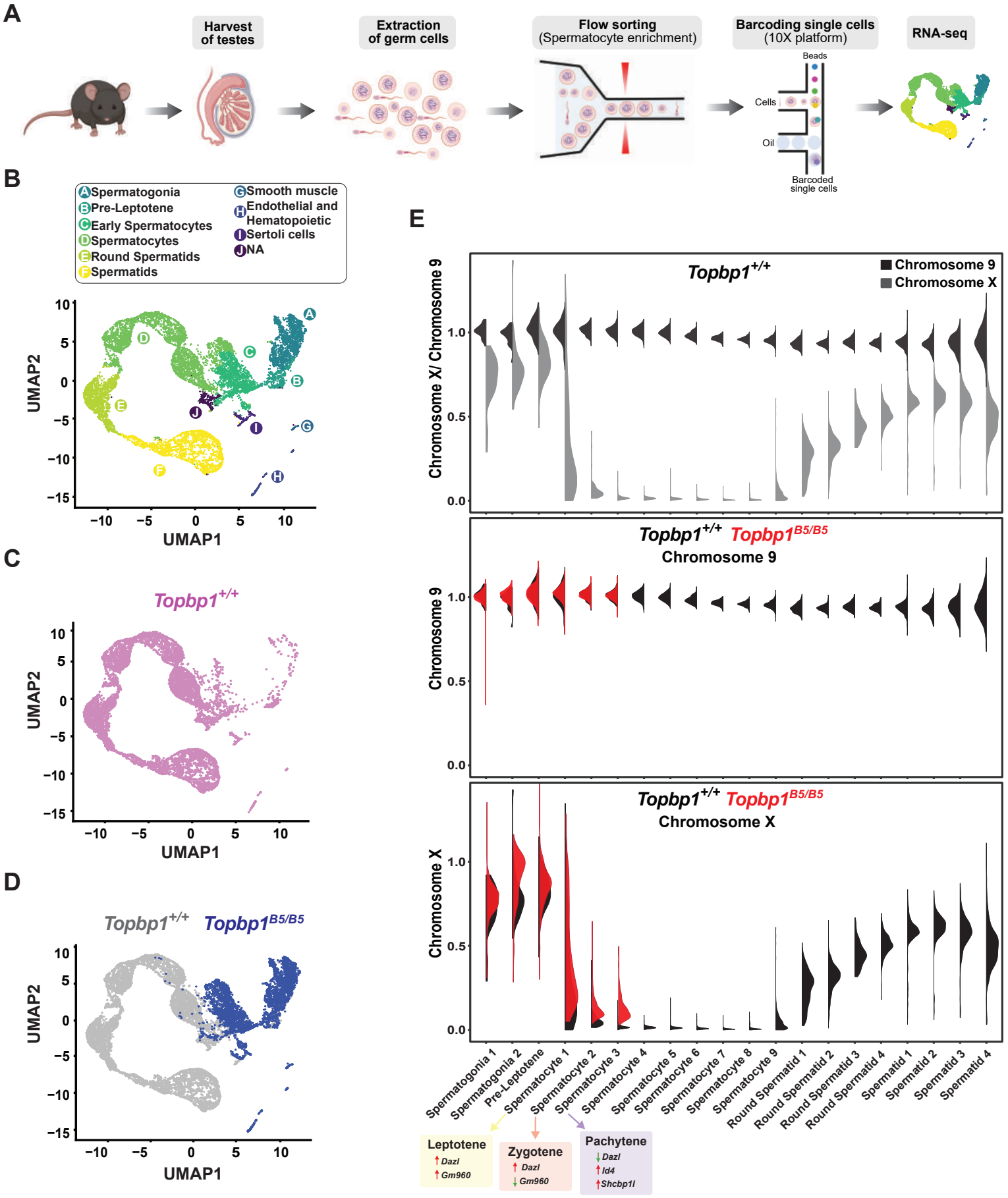
A
Harvest of testes
Extraction of germ cells
Flow sorting (Spermatocyte enrichment)
Barcoding single cells (10X platform)
RNA-seq
Beads
Cells
Oil
Barcoded single cells
B
A Spermatogonia
B Pre-Leptotene
C Early Spermatocytes
D Spermatocytes
E Round Spermatids
F Spermatids
G Smooth muscle
H Endothelial and Hematopoietic
I Sertoli cells
J NA
UMAP2
UMAP1
C
Topbp1+/+
D
Topbp1+/+ Topbp1B5/B5
E
Topbp1+/+
Chromosome 9
Chromosome X
Chromosome X/ Chromosome 9
Topbp1+/+ Topbp1B5/B5
Chromosome 9
Topbp1+/+ Topbp1B5/B5
Chromosome X
Spermatogonia 1
Spermatogonia 2
Pre-Leptotene
Spermatocyte 1
Spermatocyte 2
Spermatocyte 3
Spermatocyte 4
Spermatocyte 5
Spermatocyte 6
Spermatocyte 7
Spermatocyte 8
Spermatocyte 9
Round Spermatid 1
Round Spermatid 2
Round Spermatid 3
Round Spermatid 4
Spermatid 1
Spermatid 2
Spermatid 3
Spermatid 4
Leptotene
Dazl
Gm960
Zygotene
Dazl
Gm960
Pachytene
Dazl
Id4
Shcbp1l

Figure 7

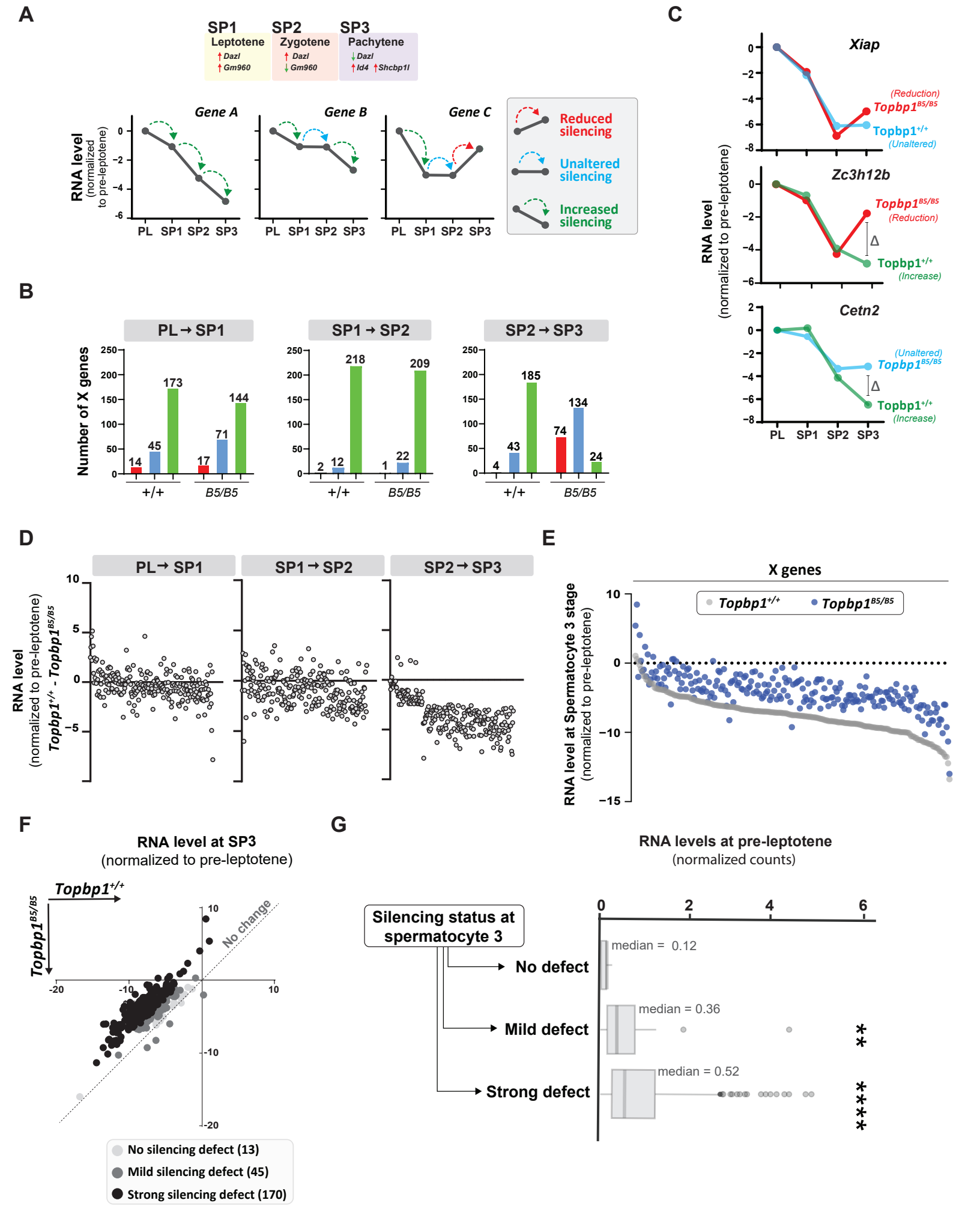
A
SP1 Leptotene
Dazl
Gm960
SP2 Zygotene
Dazl
Gm960
SP3 Pachytene
Dazl
Id4
Shcbp1l
Gene A
Gene B
Gene C
RNA level (normalized to pre-leptotene)
PL SP1 SP2 SP3
Reduced silencing
Unaltered silencing
Increased silencing
B
PL→SP1
SP1→SP2
SP2→SP3
Number of X genes
+/+
B5/B5
C
Xiap
Zc3h12b
Cetn2
(Reduction)
(Unaltered)
(Increase)
RNA level (normalized to pre-leptotene)
D
PL→SP1
SP1→SP2
SP2→SP3
RNA level (normalized to pre-leptotene)
Topbp1+/+ - Topbp1B5/B5
E
X genes
Topbp1+/+
Topbp1B5/B5
RNA level at Spermatocyte 3 stage (normalized to pre-leptotene)
F
RNA level at SP3 (normalized to pre-leptotene)
Topbp1+/+
Topbp1B5/B5
No change
No silencing defect (13)
Mild silencing defect (45)
Strong silencing defect (170)
G
RNA levels at pre-leptotene (normalized counts)
Silencing status at spermatocyte 3
No defect
Mild defect
Strong defect
median = 0.12
median = 0.36
median = 0.52

Figure 8

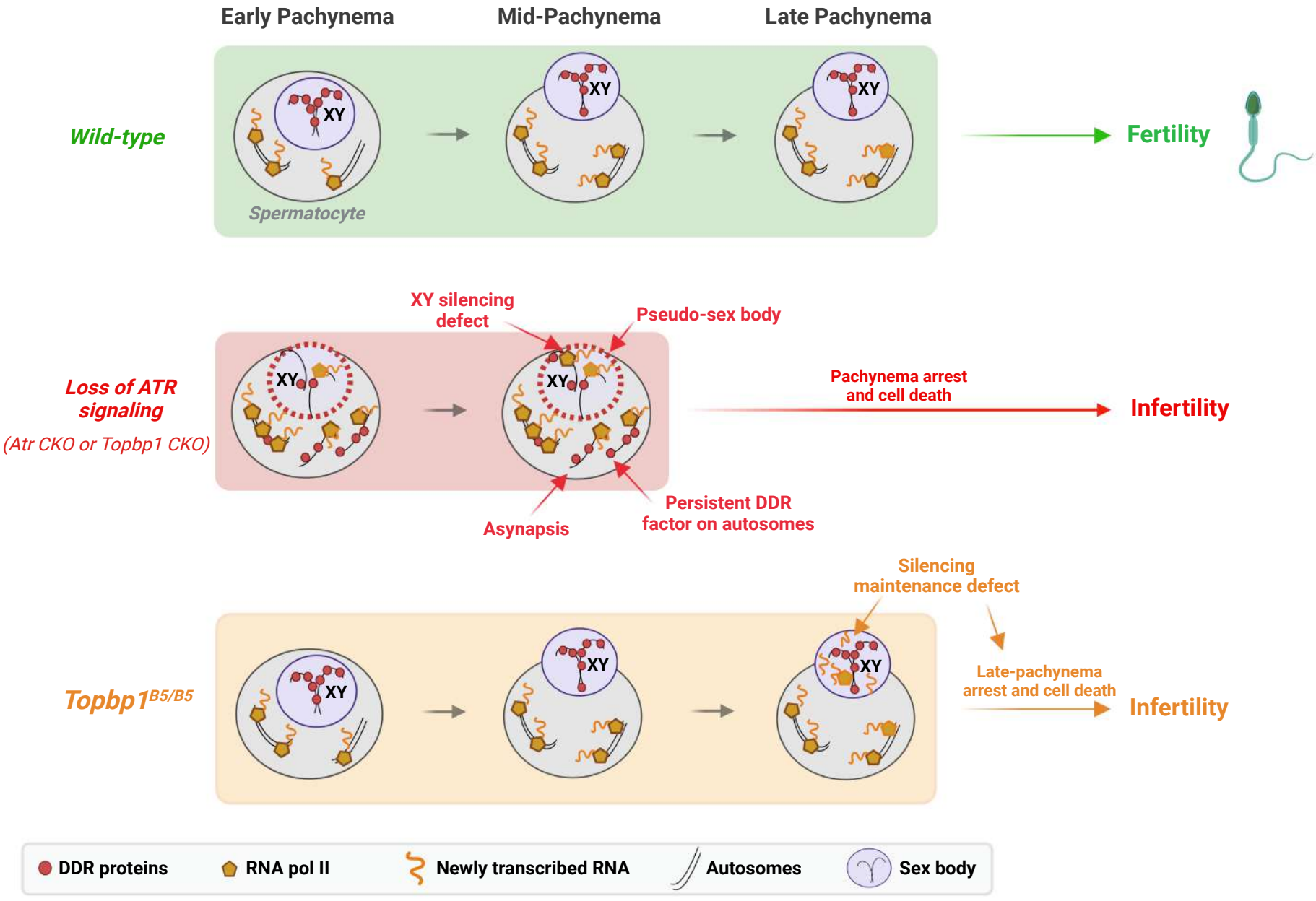
Early Pachynema
Mid-Pachynema
Late Pachynema
Wild-type
XY
Spermatocyte
Fertility
Loss of ATR signaling
(Atr CKO or Topbp1 CKO)
XY silencing defect
Pseudo-sex body
Pachynema arrest and cell death
Infertility
Asynapsis
Persistent DDR factor on autosomes
Topbp1B5/B5
Silencing maintenance defect
Late-pachynema arrest and cell death
Infertility
DDR proteins
RNA pol II
Newly transcribed RNA
Autosomes
Sex body